Revision 2

Interaction of seawater with (ultra)mafic alkaline rocks – Alternative process for the formation of aegirine

Vladislav RAPPRICH[1], Dalibor MATÝSEK[2], Ondřej POUR[1], Jakub JIRÁSEK[3], Jitka MÍKOVÁ[1], Tomáš MAGNA[1]

1 – Czech Geological Survey, Klárov 3, 118 21 Prague, Czech Republic, vladislav.rapprich@geology.cz

2 – VŠB-Technical University of Ostrava, Faculty of Mining and Geology, Department of Geological Engineering, 17. listopadu 15/2172, 708 00 Ostrava-Poruba, Czech Republic

3 – Palacký University Olomouc, Faculty of Science, Department of Geology, 17. listopadu 1192/11, 771 46 Olomouc, Czech Republic

ORCID: VR - 0000-0003-4349-2116, DM - 0000-0002-1412-1079, OP - 0000-0001-8259-4655, JJ - 0000-0002-3087-2497, JM - 0000-0001-5774-202X

Keywords: aegirine, sodic metasomatism, pyroxene re-crystallization, submarine alkaline rocks, teschenite

Abstract

Submarine mafic and relatively Na-poor alkaline rocks in the Outer Carpathians often contain aegirine, a sodic pyroxene usually found in differentiated alkaline rocks. Its presence in rocks that are too basic and Na-poor for its conventional magmatic appearance is linked to sodic alteration of submarine alkaline rocks. Aegirine crystals grow on altered rims of diopside, commonly with crystallographic unconformity, suggesting that their growth was related to alteration and that aegirine does not represent a late stage of continuous clinopyroxene

crystallization. The U-shaped REE patterns in the studied aegirine lack Eu anomaly, characteristic for aegirine from differentiated alkaline rocks. Therefore, the involvement of chemically more evolved magma is unlikely to have played any role in the formation of aegirine in ijolites and essexites. Formation of aegirine in submarine alkaline rocks may thus represent an alternative process to spilitization. However, this process is strongly limited by the availability of Fe^{3+} oxidized and mobilized by hydrothermal alteration, which may explain a relative scarcity of aegirine observed in submarine alkaline rocks compared to near-complete albitization of spilites, and its absence in high-MgO rocks (> 10 wt%). Due to the blocking effect related to Fe^{3+} unavailability, ijolites and essexites do not display significant Na enrichment. We posit that Na incorporated in aegirine was mainly sourced from the zeolitized interstitial glass.

1. Introduction

Aegirine (nominally $NaFe^{3+}Si_2O_6$) is a member of the clinopyroxene group and forms green to greenish-black zoned crystals displaying strong green to brown pleochroism. It mainly occurs in differentiated alkaline rocks (alkaline granites/rhyolites, foid syenites, phonolites, leucocratic foidites and related pegmatoid rocks) in the association with sodic amphibole, alkali feldspar and nepheline or quartz (e.g., Yagi 1966; Larsen 1976; Pazdernik 1997; Piilonen et al. 1998; Baudouin et al. 2016). Aegirine was also frequently reported in high-pressure low-temperature metamorphic rocks such as greenschist, blueschist and epidote-amphibolites (e.g., Banno and Yamada 2012; Flores et al. 2015; Ghose et al. 2021), as a product of sodic metasomatism - fenitization (e.g., Sutherland 1969; Cooper et al. 2016; Weidendorfer et al. 2016), as authigenic phase resulting from diagenesis/anchimetamorphism

of marine sediments (e.g., Fortey and Michie 1978; McSwiggen et al. 1994), and in Na-rich magmatic rocks including carbonatites (e.g., Woolley et al. 1995; Chakhmouradian and Mitchell 2002; Ackerman et al. 2021). Its hydrothermal origin at temperatures around ~200°C was experimentally proven as well (Decarreau et al. 2004). In magmatic systems, it usually crystallizes at lower magmatic temperatures, close to the solidus of differentiated alkaline melts at a high oxygen fugacity (e.g., Yagi 1966; Mann et al. 2006). The presence of aegirine in (ultra)mafic alkaline rocks may imply (i) extensive differentiation during crystallization of mafic magma (e.g., Weidendorfer et al. 2016), or (ii) a mingling/mixing process involving a batch of a differentiated alkaline melt (e.g., Chakhmouradian and Mitchell 2002). Neither of these modes of the formation of aegirine is likely applicable to (ultra)mafic alkaline rocks with no other signs of differentiation or mixing with chemically evolved melts and with relatively limited contents of Na_2O.

In the Bohemian Massif and the Outer Carpathians (Central Europe), aegirine was found in Mesozoic alkaline mafic to ultramafic rocks (e.g., Ulrych et al. 1996; Dolníček et al. 2010) although it normally crystallizes from differentiated alkaline melts. Aegirine occurs in the so-called Teschenite Association Rocks (TAR; Menčík et al. 1983), submarine alkaline rocks of the Outer Carpathians, but is much less frequent compared to diopside. Aegirine was, for the first time in the TAR, reported by Pacák (1926) from several localities. He mentioned continuous compositional mixing series between both aegirine – aegirine-augite and aegirine – augite. However, such observations were solely based on the optical microscopy with no in situ micro-analytical technique available at that time, and should be treated with precaution.

In this study, we focused on the appearance and chemistry of aegirine of TAR occurrences in the Moravia and Silesia regions (NE Czech Republic), to unravel the origin and possible petrogenetic significance of aegirine in submarine mafic alkaline rocks. We also attempted to

interpret whether aegirine can provide further constraints on the interaction of mafic alkaline melts with the ambient environment.

2. Geological setting

The Cretaceous mafic alkaline rocks studied here and known as the Teschenite Association Rocks (TAR; Menčík et al. 1983), are embedded as lavas or penetrate as dykes and sills into the Early Cretaceous sedimentary sequences of the Outer Carpathians. The Outer Flysch Carpathians represent the most external zone of the Carpathian mountain chain, which is a part of the Alpine–Carpathian–Dinaridic orogenic system (Schmid et al. 2008) extending over southern and southeastern Europe. The Outer Flysch Carpathians, extending from eastern Czech Republic to southern Poland, comprise folded and thrusted strata of the latest Jurassic to the Lower Miocene. In their present form, the Outer Flysch Carpathians consist of two groups of nappes (Fig. 1): the Outer Group of Nappes (divided from the lowest to highest into the Pouzdřany, Ždánice-Subsilesian, Silesian and Foremagura nappes/units), and the Magura Group of Nappes. The entire nappe allochthons were thrusted more than 60 km over the Miocene sediments of the Carpathian Foredeep (Picha et al. 2006).

The Silesian Nappe consists of Late Jurrasic to Oligocene, predominantly flysch sediments deposited in the Silesian Basin (Menčík et al. 1983; Picha et al. 2006). They represent marine sediments of the carbonate platform, continental slope, and deep-ocean floor. Since the areal extent of the unit is large – just in the Czech territory it forms an irregular belt *ca* 120 km long and up to *ca* 20 km wide, three facies (or subunits) differing in the stratigraphy and structures are recognized: Godula (ocean floor), Kelč (frontal slope), and Baška (shelf) facies. For the most significant Godula Facies, nine lithostratigraphic units (formations) were defined (Eliáš

et al. 2003), including the Hradiště Formation (Menčík et al. 1983), which comprises numerous small volcanic bodies of TAR (Fig. 1).

The rocks of TAR are largely described as sills in the un-metamorphosed Alpine-type refolded sediments that include the volcanic bodies. The sill thickness is highly variable, ranging from tens of centimetres to approximately 30–40 m (e.g., Włodyka 2010). Szopa et al. (2014) emphasized that shallow subvolcanic intrusions prevail in the Polish part of the belt, but lavas and associated volcaniclastic deposits occur in the Czech part of the region as well. Volcanic activity has been dated, based on micro- and macro-paleontological evidence from the contact-metamorphosed sediments, to the Valanginian–Aptian (Hradiště Formation in the regional stratigraphy; Eliáš et al. 2003). The Ar–Ar amphibole dating yielded ages in the range 122.3–120.4 Ma (Lower Aptian: Lucinska-Anczkiewicz et al. 2002), which well fits into the age-span of 126.5–103.0 Ma obtained from U–Pb apatite dating (Szopa et al. 2014). Both geochronological methods are also consistent with the biostratigraphy.

The TAR rocks are characterized by highly variable mineral proportions as well as variable structural and textural features and a wide range of post-volcanic alterations. Petrographic classification of the IUGS (Le Maitre et al. 2002) considers the term teschenite to be a synonym for analcime gabbro (< 10% alkali feldspar), but the variability of rocks regarding the composition and textures as well as smooth transitions among single TAR rock types make the classification significantly more complicated (e.g., Machek and Matýsek 1994). Moreover, analcime as a zeolite-group phase is not a primary magmatic phase and its role in the classification of magmatic rocks should be re-considered. Historically, the term teschenite has been far more broadly used (including foid syenite, foid monzosyenite, foid monzogabbro, or even foid gabbro). Apart from phaneritic types with gabbroic appearance, the TAR also includes alkali lamprophyres (camptonite, monchiquite, fourchite, ouachitite) and fine-grained porphyritic types of effusive or near-surface intrusive bodies.

Analcimization, chloritization, smectitization and carbonatization are the most frequent processes taking place during TAR alteration. Even the contact-metamorphosed sediments in the vicinity of TAR intrusive bodies sometimes carry the apparent signs of analcimization (Matýsek 1992). Despite extensive alteration, the composition of TAR corresponds to the alkaline suite of ocean island basalt (OIB) affinity derived from the mantle via low-degree partial melting (e.g., Dostal and Owen 1998).

Aegirine usually is present in the form of coatings on larger phenocrysts of diopside and/or amphibole, but sporadically also forms thin needle-like crystals and aggregates in the groundmass. While Włodyka (2010) reported a continuous compositional trend from calcic pyroxenes towards aegirine considered as an indicator of peralkaline melt compositions, Dolníček et al. (2010) concluded that aegirine crystallized from residual NaCl-rich magmatic brines following the main magmatic crystallization stage. The aegirine crystallization temperatures were estimated by Dolníček et al. (2010) at 390–510 °C. Similarly, secondary nature of aegirine and aegirine-augite rims on diopside in TAR-related monchiquite in Cieszyn-Boguszowice (Poland) was revealed by Szopa et al. (2014). A post-magmatic origin of aegirine-augite/aegirine coatings on diopside in the leucocratic dykes and nests within the Řepiště teschenite (Czech Republic) was also determined by Kropáč et al. (2020). These authors supposed that aegirine crystallized from NaCl-rich hypersaline aqueous solutions exsolved after the main magmatic crystallization phase.

3. Materials and methods

In the studied area, the occurrences of aegirine and aegirine-augite have recently been documented from numerous sites, mostly in the form of radial sprays of needle-shaped crystals, rather homogenous in BSE images (Figs 2a–d). Less frequently, aegirine occurs as

outer growth-zones and caps on the termination of older clinopyroxene crystals. At some places, we also recognized euhedral crystals of aegirine and aegirine-augite, usually with chemical zoning visible in BSE (Fig. 2e). At a limited number of outcrops, aegirine is also present in the form of well-developed needle-like crystals in miarolic cavities, usually filled by post-volcanic calcite (Fig. 2f). We have selected representative samples containing aegirine and aegirine-augite in six localities from over 40 inspected outcrops distributed across the aerial extent of the TAR, where samples were collected. Compact aegirine crystals were preferred instead of radial aggregates because they are more suitable for detailed analytical work, including laser ablation ICPMS. The location and basic mineralogical composition of individual samples are given in Tab. 1.

Sample **TG05** represents a smaller dyke intruded into sedimentary (roughly syn-volcanic) claystones, capped with a volcanic sequence of Petřkovická hora. This dike has been classified as a devitrified augitite (Pour et al. 2022). The Stříbrník locality (sample **TG13**) is a sill intruded into the flyschoid sediments of the Hradiště Formation, which is naturally exposed in the Stříbrník creek gorge. The rock from this locality was formerly classified as fourchite (Šmíd 1978) or teschenite (Dolníček et al. 2010). Another TAR sill (collected as sample **TG15**) intruding into the Hradiště Formation sediments crops out in a gorge of a small unnamed tributary of Tichávka creek. This body was not formerly described. Another outcrop of TAR intrusion into the Hradiště Formation sediments is exposed in the Tichávka creek bottom and banks (sample **TG22**), close to the TG15 sampling site. This occurrence is well known since early 20th Century (Pacák 1926), who noticed large titanite crystals (up to 7×3 mm) in this rock. Earlier, this rock was classified as a lamprophyre due to accessory biotite (Šmíd 1978), but it was subsequently re-labelled as teschenite without further details (Dolníček et al. 2010; Kropáč et al. 2017). Kropáč et al. (2017) described aegirinization related to the walls of secondary calcite veins cross-cutting the rock. Brunarska and

Anczkiewicz (2019) provided an age of 123.7 ± 2.1 Ma, based on U–Pb dating of large titanite crystals. A leucocratic coarse-grained phaneritic pyroxene-rich sample **TG25** was collected from a historical rubbled outcrop near Borošín. Pacák (1926) described nepheline and hydronepheline from this locality but these phases were not confirmed in the studied samples. The sample **TG37** was collected at Perná, where TAR sill is exposed in the Žebrák creek gorge. Likewise the other sites, the sill intrudes into the sediments of the Hradiště Formation.

3.1.Mineral proportions

The mineral composition of studied rocks was analysed by employing x-ray diffraction (XRD) housed at the Department of Geological Engineering, VŠB-Technical University of Ostrava. The XRD analyses were carried out using a Bruker-AXS D8 Advance instrument with a θ/2θ measurement geometry and the position-sensitive detector LynxEye under the following conditions: radiation CuKα/Ni filter, 40 kV current, 40 mA voltage, step mode with a step size of 0.014° 2θ, a counting time of 0.25 seconds per step, and acquisition of five independent measurements. The qualitative analysis of diffraction patterns was performed using the EVA software (Bruker-AXS) and the database PDF-2, release 2021 (International Centre for Diffraction Data). The Rietveld method using the TOPAS software, version 5 (Bruker) was applied to verify the analyses, quantifications and to compute the unit cell parameters of mineral phases.

3.2.BSE imaging and mineral phase identification

Prior to *in situ* mineral chemistry analyses, the samples were inspected using a FEI Quanta 650 FEG scanning electron microscope (SEM) housed at the Department of Geological Engineering, VŠB-Technical University of Ostrava. The imaging and preliminary detection of mineral phases were made on natural (unpolished) fracture surfaces without the coating under the following conditions: 15 kV beam voltage, 3 nA current, 5–6 μm beam diameter, and a

vacuum of $<10^{-3}$ Pa. The Octane Elect Plus detector and Galaxy software (both EDAX) were used. The identification and quantification of spectral lines was performed using the decomposition method employing holographic peak deconvolution. Microphotographs were obtained with a backscattered electron (BSE) detector in chemical gradient mode under the following conditions: 10 kV beam voltage, 1 nA current, 4–5 μm beam diameter, vacuum 50 Pa.

3.3.In situ mineral chemistry – major elements

The polished and carbon-coated cylinders (2.5 cm/1 inch in diameter) of rock samples selected for further analytical work were prepared at the Czech Geological Survey in Prague. *In situ* micro-analyses of the studied pyroxenes composition were performed using a FEG-SEM Tescan MIRA 3GMU, housed at the Czech Geological Survey in Prague and equipped with two energy-dispersive spectrometers Oxford Instruments Ultim Max 100. The analyses were conducted with an accelerating voltage of 15 kV, absorbed current of ≈3 nA, and a working distance of 15 mm. Counting times were 15 s. For quantitative analyses SPI mineral block standards were used (jadeite (Na Kα, Al Kα), forsterite (Mg Kα), quartz (Si Kα), baryte (S Kα, Ba Lα), tugtupite (Cl Kα), orthoclase (K Kα), diopside (Ca Kα), rutile (Ti Kα), rhodonite (Mn Kα) and almandine (Fe Kα)). Analyses were processed using the Aztec 6.0 software (Oxford Instruments). The method of Vieten and Hamm (1978) balancing the deficiency of oxygen atoms corresponding to 4 cations (with all iron as Fe^{2+}) was used for the calculation of Fe^{3+} contents in clinopyroxenes.

3.4.In situ mineral chemistry – trace elements

The trace element contents of the studied pyroxenes from TAR were determined at the Czech Geological Survey in Prague using an Agilent 7900 quadrupole (Q)-ICPMS (Agilent Technologies Inc., USA) coupled with an Analyte Excite Excimer 193 nm LA system (Photon Machines, USA), equipped with a two-volume HelEx ablation cell. In total, 33 masses were

This is the peer-reviewed, final accepted version for American Mineralogist, published by the Mineralogical Society of America.
The published version is subject to change. Cite as Authors (Year) Title. American Mineralogist, in press.
DOI: https://doi.org/10.2138/am-2023-8928. http://www.minsocam.org/

monitored (^{27}Al, ^{28}Si, ^{44}Ca, ^{45}Sc, ^{51}V, ^{53}Cr, ^{55}Mn, ^{56}Fe, ^{85}Rb, ^{88}Sr, ^{90}Zr, ^{93}Nb, ^{139}La, ^{140}Ce, ^{141}Pr, ^{146}Nd, ^{147}Sm, ^{153}Eu, ^{157}Gd, ^{159}Tb, ^{163}Dy, ^{165}Ho, ^{166}Er, ^{169}Tm, ^{172}Yb, ^{175}Lu, ^{178}Hf, ^{204}Pb, ^{206}Pb, ^{207}Pb, ^{208}Pb, ^{232}Th and ^{238}U). The laser beam diameter was 35 μm. The applied laser fluence was 9.42 J·cm^{-2} with a pulse rate of 10 Hz. A typical analysis consisted of background acquisition (gas blank, 20s), sample ablation (40s), and wash-out (40s). The internal standardization was based on ^{28}Si and ^{44}Ca concentrations determined using SEM. The NIST 610 and 612 reference glass wafers (Jochum et al. 2011) were used for external calibration. These wafers were analyzed at the beginning and at the end of the analytical sessions, and after every five measurements of unknown samples to monitor the instrumental drift. The Iolite 4.0 software package (Paton et al. 2011) was used for data reduction to calculate the trace element concentrations, analytical errors, and detection limits.

3.5.Bulk-rock chemistry

The whole-rock samples of studied rocks were crushed in a steel jaw-crusher and pulverized in an agate box. Major element analyses were carried out at the Czech Geological Survey laboratories. The analytical methods included atomic absorption spectrometry, photometry and titration with complexon III, following the methodology described in Dempírová et al. (2010). For trace element concentration analysis, aliquots of powdered samples were decomposed in a mixture of 27 M HF–15M HNO_3 (6:1 v/v) in closed Teflon vials at 130 °C for 72 h. The solutions were then evaporated to incipient dryness and treated three times with small quantities of 15 M HNO_3. Thereafter, dried residues were administered with 6M HCl and equilibrated at 80 °C for 24 h. Trace element concentrations in solutions were obtained using an Agilent 7900x ICPMS. Reference materials BHVO-2 (Hawaiian basalt, USGS) and JB-2 (arc basalt, GSJ) were prepared together with unknown samples, and their trace element abundances were in agreement with published values (Jochum et al. 2005).

The bulk-rock as well as mineral chemistry data were processed and visualised using GCDkit software (Janoušek et al. 2006).

4. Results

4.1.Petrology

The devitrified augitite **TG05** is characterized by fine-grained porphyritic (originally probably vitrophyric) texture containing small diopside phenocrysts (1 mm) accompanied with dimmed pleochroic (light to dark brown) amphibole rarely >0.5 mm in length, both enclosed in a heterogeneous matrix. The matrix appears to represent devitrified glass and contains diffusively bordered colorless analcime, which is interpreted as a devitrification product (Pour et al. 2022). The rest of the matrix consists of radially arranged laths of albite and microcline (Fig. 3a), resembling spherulites known from silica-rich volcanic rocks (e.g., Breitkreuz 2013 and references therein). The thicker nature of feldspar laths in the observed radial aggregates and the absence of regular (oval) borders of these aggregates (probably due to higher diffusion rates in mafic and low-viscosity hot-glass) makes them less lucid compared to common spherulites. Nevertheless, these radial aggregates most likely also represent devitrification features. Aegirine can be found as small crystals emerging from partly altered diopside (Fig. 3a), but it is also present as sprays of acicular crystals in the zeolitized matrix (Fig. 4a).

The compositional variability of a zoned sill exposed in the Stříbrník creek gorge (sample **TG13**) is apparent at a macroscopic outcrop scale – the darker outer parts are rich in biotite, whereas the coarse-grained central part is dominated by clinopyroxene. The rock has an intersertal texture with larger phenocrysts of diopside (several mm), and smaller crystals of biotite, apatite and anatase surrounded by originally glassy groundmass (Fig. 3b). The

devitrification of original glass in the groundmass is indicated by radial aggregates (resembling spherulites) of microcline and albite enclosed in analcime and calcite (Fig. 4b). Accessory altered Ti–Fe oxides and skeletal titanite can be also found. Despite the subsequent zeolitization, the devitrification mineral assemblage suggests that the rock would originally (if not quenched to form glass) crystallize plagioclase in association with nepheline, classifying this rock as foid gabbro or foid monzo-gabbro (essexite). Such assumption is further supported by the position of sample TG13 in TAS diagram (Le Maitre et al. 2002: Fig. 5a), complemented by the discrimination diagram of Ti/Zr vs. Nb/Y (Pearce 1996: Fig. 5b) based on the systematics of relatively immobile elements. Aegirine is present in the form of smaller crystals growing on the pyramidal edges of pre-existing diopside phenocrysts, or partly coating these phenocrysts (Figs 3b and 4b). It is noteworthy that aegirine is clearly separated from the diopside stage by a zone of significant alteration.

The sample **TG15** is characterized by a rather phaneritic texture comprising large crystals of diopside (exceeding 5 mm; Fig. 3c), and somewhat smaller amphibole and biotite crystals. Despite unusually high abundance of apatite (18 wt%) revealed by quantitative X-ray diffraction (Table 1), the rock contains only 5.4 wt% P_2O_5 (see Electronic Supplementary Material – ESM1 – for bulk-rock chemistry). This discrepancy in analytical data, checked six times on two diffractometers at two different institutions, is probably caused by anomalous porosity of the apatite crystals. They are extremely rich in pores less than 5 μm in size, following the crystal planes. In fact, they might be primary fluid (gaseous) inclusions. Such porosity affects mineral phase quantification because the Rietveld method does not account for the empty space within the crystals, while their absorption coefficients differ significantly. Possible influence of the micro-absorption of the X-ray was minimized by the micronizations. Large amounts of apatite (over 10 wt%) and maghemite (5 wt% - see Tab. 1), combined with heterogeneously distributed but abundant titanite, are responsible for the low silica content

(29 wt%). Possible original glass in smaller pockets enclosed among larger crystals was replaced by analcime, calcite and siderite (Fig. 3c). The silica super-undersaturation makes the primary origin of the observed plagioclase rather doubtful and the high phosphorus content points toward phoscoritic affinity of this rock, hereafter labelled as phoscoritic ijolite. Aegirine occurs as series of needle-shaped crystals emerging from the tips of partly altered diopside phenocrysts (Fig. 3d).

The sample **TG22** from the Tichávka creek has an intersertal texture with large diopside (up to 3 mm) phenocrysts associated with amphibole, biotite, apatite, titanite and magnetite (ulvöspinel - partly decomposed to anatase and hematite) enclosed in groundmass with radial aggregates of secondary albite with microcline surrounded by analcime, calcite and chlorite (Fig. 3e). The texture and composition of groundmass suggest its origin from devitrification of original glass. Given the low silica content (Fig. 5a) and large proportion of analcime (as zeolite analogue to nepheline), we classify this rock as zeolitized (analcime) ijolite. Anhedral aegirine is present in the matrix as well as euhedral crystals attached to the altered surface of diopside phenocrysts (Fig. 3e).

Leucocratic coarse-grained phaneritic to intersertal pyroxene-rich sample **TG25** from Borošín is distinguished by predominant zeolite, as natrolite dominates over analcime. Transition of the whitish to colourless natrolite into cloudy groundmass reflects the admixture of finely dispersed K-feldspar, kaolinite and chlorite. Diopside phenocrysts (several mm) are associated with less abundant and smaller (<0.5 mm) biotite crystals, locally partly encapsulating diopside (Fig. 3f). Based on the comparison of the mineral assemblage (Tab. 1) with the chemical composition (Fig. 5a), the rock was classified as zeolitized (natrolite) essexite (foid gabbro). Previously described hydronepheline (Pacák 1926) appears to correspond to massive natrolite without acicular structure (e.g., Dunham 1933), possibly pseudomorphing after the original nepheline. Aegirine is very frequent and forms either

316 euhedral wedge-shaped crystals usually attached to slightly altered diopside (Fig. 3f), or radial
317 aggregates enclosed in natrolite or matrix (Fig. 3g), or even emerging into the miarolic
318 cavities (Figs 4c,d).

319 The crystal-size variability across the body (finer-grained margins and coarser-grained core)
320 is clearly visible at the outcrop of the TAR sill sample **TG37** at Perná. Coarse-grained
321 camptonite of this sill differs from the other studied rocks by the predominance of amphibole
322 over clinopyroxene (Fig. 3h). Amphibole and diopside (with thin hedenbergite rims) are
323 associated with partly to totally altered plagioclase (andesine to labradorite), with relatively
324 fresh cores mantled with prehnite, analcime and K-feldspar. Apatite is the most common
325 accessory phase. Aegirine is present in the form of lath-shaped crystals in the matrix,
326 accompanied by K-feldspar and analcime, or as coatings on amphibole and clinopyroxene
327 (Fig. 3h). In contrast to diopside from the other samples in this study, diopside from
328 camptonite TG37 is characterized by well-developed sector zoning and continuous
329 hedenbergite rims encircling the entire diopside phenocrysts (Figs 4e,f).

330 The studied rocks containing aegirine as well as the entire TAR suite (see ESM1) belong to
331 the alkaline rocks extending in the TAS diagram (Fig. 5a; Le Maitre et al. 2002) from the field
332 of foidites (foidolites), across the basanite/tephrite (foid gabbro) field to the field of phono-
333 tephrites (foid monzo-gabbro). Although the TAR suite comprises picritic rocks (picrobasalts,
334 picrites, meimechites), these highly magnesian rocks lack any detectable aegirine. Few
335 samples plotting near the zero alkali content appear to be the result of post-magmatic
336 alteration/weathering. As the rocks are significantly affected by zeolitization and their volatile
337 contents (H_2O^+, H_2O^-, CO_2) range 1.9–14.6 wt% (strongly carbonatized olivine nephelinite
338 TG45 with up to 20.6 wt%; see ESM1), their geochemical character was also monitored using
339 the Zr/Ti *vs.* Nb/Y classification diagram based on the systematics of relatively immobile
340 trace-elements (Fig. 5b; Pearce 1996). In this plot, the data form a tight cluster on the

boundary between the fields of alkali basalts (foid gabbros) and foidites (foidolites). Although the samples experienced significant zeolitization, the entire suite does not display sizeable Na enrichment. Most of the samples are arranged in a simple trend with negative correlation between Na_2O and MgO (Fig. 5c). Several samples depart from the general trend to lower Na contents and only the sample TG25 is characterized by an increased Na content deviating from the general trend.

4.2.Pyroxene mineral chemistry

The analysed pyroxenes display a significant difference in the chemical composition (see Electronic Supplementary Material – ESM2). The unaltered relicts of the primary clinopyroxene phenocrysts plot in the field of quadrilateral pyroxenes in the Q–Jd–Ae diagram (after Morimoto 1988; Fig. 6a), whereby only the outer rims of the larger phenocrysts from camptonite TG37 cross into the aegirine-augite field. The quadrilateral pyroxene is further classified mostly as pure diopside in the En–Wo–Fs diagram (Morimoto 1988; Fig. 6b). Some analyses plot above the Wo_{50} line as a result of Ca overestimation due to the substitution of Ca-Tschermak´s molecules replacing diopside molecule. This effect is common in alkaline rocks (e.g., Rapprich 2005 and references therein). The secondary crystals grown on the tips of the primary phenocrysts as well as the radial sprays then fall mostly in the field of aegirine or, to a lesser extent, also to the aegirine-augite field (Fig. 6a). There is no clear difference between the crystals emerging from diopside phenocrysts and the radial sprays, but the significant gap between both generations (diopside and aegirine) is apparent. This compositional gap is well pronounced also in the distribution maps of selected elements, even if the phenocryst surface consists of a hedenbergite to aegirine-augite rim (Fig. 7).

The two observed generations of pyroxene differ strikingly also in the trace element contents, namely in REE patterns (Fig. 8a). The primary diopside crystals display smooth REE patterns

parallel to the composition of the respective bulk-rocks with LREE relatively enriched compared to HREE. This trend deviates only for La–Pr with the increasing depletion from Pr to La. The aegirine crystals show a completely reverse trend with U-shaped patterns (Fig. 8a). The depletion in MREE and the enrichment in LREE and HREE correspond neither to the bulk-rock nor to the diopside trends. Both populations lack the Eu anomaly.

Significant differences can also be observed for other incompatible trace elements (Fig. 8b), where bulk-rock analyses reveal a good correlation with average OIB. While the primary diopsides are strongly depleted in highly incompatible elements (Rb to Nb) with the weakly incompatible elements (Nd to Lu) rather following the bulk-rock trends, the secondary aegirines display a distinctively different trend. Depletion in highly incompatible elements is not so pronounced and its degree is similar to that observed for the weakly incompatible elements. On the other hand, the aegirine is enriched in incompatible elements preferentially mobile in the melt (high-field strength element: HFSE, here represented by Nb and Zr), whereas fluid-mobile incompatible elements (large-ion lithophile elements: LILE, here represented by Rb and Sr) are depleted. The HFSE trend is partly reflected also by Ti, but incorporation of Ti into the crystal lattice of pyroxene is pressure-controlled (e.g., Tracy and Robinson 1977; Haloda et al. 2010), and the evaluation of this element is thus more complex. The described elemental pattern of aegirine is even more pronounced in the case of aegirine radial sprays in the zeolitized groundmass (Fig. 8b).

5. Discussion

5.1.Genetic relations between diopside and aegirine

The critical question regarding the presence of aegirine in Na-poor and highly magnesian rocks rises about its late-magmatic *vs.* post-magmatic origin. Some studies (e.g., Włodyka

2010) suggested rather continuous crystallization from diopside towards aegirine in the TAR. According to the full solid-solution between diopside and aegirine (e.g., Yagi 1966; Yoshikawa 1977; Redhammer et al. 2012), continuous magmatic crystallization is reflected by rather continuous compositional trends observed in zoned clinopyroxenes of peralkaline rocks, i.e. agpaitic syenites and tinguaites (Filina et al. 2017; Batki et al. 2018). These occurrences are characterized as continuous rims encircling the entire clinopyroxene phenocryst (Filina et al. 2017). Aegirine-rich aegirine-augite described from zeolitized ijolite pegmatite at La Madera, Argentina (Galliski et al. 2004), occurs in spherical structures in association with zeolites, separated from primary diopside or aegirine-poor aegirine-augite, and its magmatic origin is rather doubtful. Focusing in the first step on textures, our observations appear to confirm possible continuous crystallization of aegirine over diopside and hedenbergite solely in the case of camptonite TG37. This sample represents a more evolved member of the suite, where early diopside core has a hedenbergite rim coated with aegirine (Fig. 7), very similar to the observations provided by Filina et al. (2017) from Kola syenites. Unlike the other samples, the aegirine coating is almost continuously enveloping the entire phenocryst (in many cases even glomerocrysts – Fig. 3h). Crystallization hiatus may not be excluded, but the diffuse transitions on diopside/hedenbergite and hedenbergite/aegirine boundaries (Fig. 7) imply a rather progressive change in the residual melt composition, controlling the chemistry of crystallizing pyroxene. This assumption is also supported by the absence of any alteration zone, developed in other samples between diopside phenocrysts and aegirine.

All studied samples (except TG37) are characterized by a distinct aegirine appearance. Aegirine mostly forms small euhedral prismatic crystals or aggregates of parallel fibres growing from a partly altered diopside phenocryst. Bladed or parallel fibres of aegirine growing from diopside phenocrysts were described by Chakhmouradian and Mitchell (2002)

415 from a contact of nepheline microsyenite with alkaline pegmatite. However, in the case of the
416 TAR aegirine occurs in a homogeneous mafic rock, without petrographic or geochemical
417 evidence of a distinct magma batch. The aegirine crystals grow into the zeolitized groundmass
418 surrounding the diopside phenocrysts, or form radial sprays in the groundmass. The studied
419 aegirine crystals are usually separated from fresh diopside by an altered rim of the diopside
420 phenocrysts (see Figs 3b–e, 4b), or eventually crystallized on completely altered diopside
421 (Fig. 4a). In addition, the aegirine c-axis often is rotated from the orientation of the diopside
422 c-axis (e.g., Figs 3e, 4e). This appearance suggests that aegirine crystallized subsequently to
423 the alteration of diopside, apart from the main magmatic crystallization series. In the case of
424 aegirine crystallizing from residual interstitial (chemically evolved) melt and subsequent
425 alteration, the alteration envelope would enclose both diopside and aegirine, which is
426 inconsistent with the observations (Figs 3b–e, 4b). Besides the textural examinations, the
427 crystallization delay between diopside and aegirine can also be deduced from a significant
428 compositional gap (Fig. 6), which contrasts with rather continuous compositional trends
429 observed in rocks with clinopyroxene composition evolving from diopside/hedenbergite to
430 aegirine-augite/aegirine (Filina et al. 2017; Batki et al. 2018). Last but not least, post-
431 magmatic origin of aegirine in the studied rocks may also be deduced from its association
432 with other alteration and re-crystallization mineral phases, namely zeolites (Fig. 3).

433 Beside the smaller euhedral crystals, the sample TG25 contains radial sprays of needle-shaped
434 aegirine crystals (Figs 3d, 4c,d). These may, to some extent, resemble clinopyroxene
435 spherulites formed in super-cooled basaltic andesite submarine lava on the Pacific-Antarctic
436 Ridge (Monecke et al. 2004). Unlike the calcic clinopyroxene, aegirine may crystallize and
437 grow at lower temperatures (down to 200°C for aegirine [Decarreau et al. 2004] vs
438 suprasolidus temperatures for diopside), which may explain its thicker shapes compared to
439 fibrous aggregates described by Monecke et al. (2004). While the clinopyroxene spherulites

crystallized from hot glass at the temperatures above the glass transition (~2/3 of solidus T), the aegirine radial sprays are enclosed in the zeolitized groundmass and in some cases are also developed into open space on cracks or in cavities (Fig. 2f). This indicates a much wider range of conditions for the growth of these aegirine aggregates from early stages of groundmass (possibly glassy in original stage) alteration (prior to zeolitization) to the late stage crystallization from fluids into voids.

The history of aegirine experimental synthesis lasts for almost 100 years (see summary given by Decarreau et al. 2004), suggesting that aegirine may crystallize under a wide range of temperatures and pressures, requiring several hours to several days for synthesis. The experimentally proven aegirine synthetization/crystallization temperature has dropped during last two decades from ca 200 °C (Decarreau et al. 2004) to as low as 130 °C (Redhammer et al. 2019). Low temperatures of the formation of natural aegirine were also indicated. The earlier study of the fluid inclusions hosted by aegirine in the zeolitized ijolite from Tichá (equals to our sample TG22) revealed crystallization temperatures of aegirine in the range 390–510 °C (Dolníček et al. 2010), far below the solidus of an ijolitic melt (modelled to ca 840 °C for a compositionally similar ijolite given in Haloda et al. 2010).

Both pyroxene generations, i.e. diopside and aegirine, differ significantly in REE patterns (Fig. 8a). The smooth but relatively steep pattern lacking any Eu anomaly with relative depletion of LREE (La, Ce, Pr) indicates the equilibrium crystallization of diopside from an ijolitic or similar melt, resulting in the enrichment of the residual melt in these LREE (e.g., McSween et al. 1996; Eby et al. 1998; Haloda et al. 2010). The residual melt in the samples from this study was represented by interstitial glass, subsequently devitrified and/or zeolitized by hydrothermal alteration. The HREE enrichment combined with rather flat pattern from LREE to MREE is common feature of aegirine from highly alkaline rocks (e.g., Baudouin et al. 2016; Weidendorfer et al. 2016). Very commonly, the REE patterns of aegirine from

differentiated alkaline rocks follow rather U- or even V-shaped curve, but in these cases usually associated with a pronounced negative Eu anomaly, inherited from the melt composition depleted in Eu by fractionation of plagioclase (e.g., Shearer and Larsen 1994; Piilonen et al. 1998). The absence of Eu anomaly supported by the petrographic observations and the fact, that aegirine crystallized subsequently to alteration of diopside, may thus exclude any role of differentiated alkaline melt from model of the aegirine formation in TAR. On the other hand, key role of Na for crystallization of aegirine implies a possibly significant role of seawater, as a crucial reservoir of Na at the Earth´s surface. In addition, the reaction between seawater and erupted lava or high-level intrusion emplaced into poorly consolidated sediments on the seafloor results in formation of temporary hydrothermal system responsible for alteration of cooling magmatic rock.

5.2.Role of seawater in formation of aegirine

Sodic metasomatism of submarine basaltic lavas on the contact with seawater is generally referred to as spilitization and the main feature of this process is albitization of feldspar (e.g., Hyndman 1972; Rosenbauer et al. 1988). It has been geochemically proven that this process is not related to long-term low-temperature submarine weathering of solidified lavas but that it instead requires heat, usually released by a cooling lava shortly after the eruption (e.g., Vatin-Perignon et al. 1979). The spilitization is restricted to MORB-type ocean floor tholeiitic basalts in which Ca is mainly fixed in abundant plagioclase. The Na–Ca cation exchange leads to the albitization of calcic plagioclase. Alkaline basaltic rocks also erupt on the ocean floor although to a much lesser extent. A significantly lower degree of partial melting of a less depleted mantle source results in a distinct mineral composition. Instead of plagioclase, Ca is mainly fixed in abundant clinopyroxene in primitive alkaline rocks. Reaction with Na-rich seawater then may not lead to albitization, if plagioclase is not present. Instead, Na-rich fluids may attack the main Ca carrier in alkaline rocks, i.e. clinopyroxene. In this case, charge-

490 balanced aegirine substitution ($NaFe^{3+}$→CaMg) may take place instead of albite substitution
491 (NaSi→CaAl). At this point, a question may arise why the amount of aegirine in alkaline
492 rocks cannot be compared with the amount of albite in spilities. Whereas the albite
493 substitution in plagioclase-dominated rocks is (beside temperature) limited solely by Ca
494 saturation of seawater, defined by carbonate compensation depth (CCD; Ben-Yaakov et al.
495 1974), the aegirine substitution is a more complex phenomenon. Apart from Ca-
496 undersaturation of seawater, mobilized ferric, or oxidizable ferrous iron is a critical
497 requirement for building an aegirine molecule. Most Fe (both ferric and ferrous) in mafic
498 alkaline rocks is fixed in iron-oxides (maghemite, magnetite, ulvöspinel, etc. – see Figs 3c,e),
499 and those phases remain rather unaffected or only weakly altered. All Fe necessary for
500 aegirine crystallization thus has to be mobilized from altered diopside. As the whole TAR
501 suite consists of rather primitive MgO-rich rocks, the limited amount of Fe available in
502 diopside (Fig. 6b) is therefore the main limiting factor, controlling the growth of aegirine. We
503 note that no aegirine was observed in rocks with MgO>10 wt% (or Mg# > 50; Mg# calculated
504 as a molar proportion 100*MgO/[MgO+FeO^{tot}]) (Fig. 5c), although the TAR suite comprises
505 rocks with up to 26 wt% MgO. The greatest amount of aegirine (5 wt%, Tab. 1) was
506 documented in the zeolitized essexite TG25 (Mg# = 43), where it could also be detected by
507 whole-rock X-ray diffraction (Tab. 1). This sample is the only one plotting above the linear
508 differentiation trend in the MgO vs Na_2O diagram (Fig. 5c). This sample also differs from the
509 remaining samples in its position in separate nappe of uncertain facies located to the north
510 from the main belt of TAR occurrences (Fig. 1). Due to the lack of outcrops the sedimentary
511 rocks enveloping the magmatic body could not been studied, but two options are possible. 1)
512 This nappe of uncertain facies may possibly represent a deeper zone of the ocean, with lower
513 saturation of seawater with Ca, The increasing tendency to Na–Ca cation exchange between
514 seawater and a cooling magma can then be expected in deeper seawater with lower Ca-

515 saturation, around or below CCD. However, the present knowledge about the different facial
516 developments of the Silesian Unit (see Eliáš 1979) does not expect significant variations of
517 ocean depth at this stratigraphic level. 2) In particular, Godula facies of the Silesian Unit
518 consists of flysch originating in deep-water trough at the foot of the continental slope. Such
519 sedimentary environment is typical for highly variable lithologies (e.g., Johnson and Alam
520 1991; Li et al. 2021), and, therefore, each TAR locality might be unique considering the
521 surrounding sediments.

522 Based on the MgO vs Na_2O systematics (Fig. 5c) we may conclude that most Na incorporated
523 into secondary aegirine was sourced from the groundmass. From the same systematics we
524 anticipate that the zeolitization process of all samples was mainly associated with hydration of
525 the groundmass (possibly glassy) with no, or only negligible contribution of Na from
526 seawater. These assertions are also supported by the trace element patterns of aegirine with
527 significant HFSE enrichment (Fig. 8b). Strong HFSE partitioning between clinopyroxene and
528 melt during equilibrated crystallization has been documented by several studies (e.g.,
529 Weidendorfer et al. 2016; Baudouin et al. 2020) but the subsolidus groundmass re-
530 crystallization is not fully equivalent to equilibrium crystallization from melt. As HFSE
531 become enriched in the residual melt (i.e. glass) of alkaline rocks, the contribution of
532 recrystallizing glass to the formation of aegirine may well explain these patterns. On the other
533 hand, the depletion in LILE suggests a rather negligible role of seawater delivering alkalis and
534 other water-/fluid-mobile elements to the neoformed aegirine. The LILE (Rb, Sr) and also U
535 depletion in aegirine from TAR is strongly developed compared to negligible depletion or
536 even enrichment (namely Sr) in differentiated alkaline rocks (cf. Weidendorfer et al. 2016;
537 Baudouin et al. 2020).

538 Although the observed texture suggests that aegirine growth results from alteration of primary
539 diopside, significant trapping of Na (and other water-mobile elements) from seawater is

effectively blocked by the lack of mobilized Fe, particularly in MgO-rich rocks. As a result, the amount of secondary aegirine does not reach the volume of primary diopside, which contrasts with the commonly complete albitization of spilites. The role of the (heated) seawater in the aegirine formation appears to be restricted mainly to alteration of primary diopside, destabilization of primary glass and oxidation of the available ferrous iron into ferric iron. The entire process can then be summarized as follows: 1) the original mafic alkaline rock with diopside phenocrysts enclosed in nephelinitic/glassy groundmass (Fig. 9a) undergoes intense alteration due to contact with seawater (Fig. 9b). 2) secondary aegirine forms from available Fe^{3+} which is sourced from altered diopside and from Na which is sourced from altered glass and/or nepheline (Fig. 9c), while the supply of seawater cations is blocked by the lack of Fe^{3+}.

In the global perspective, the absence of spilitized submarine mafic alkaline lavas is related to the mineral assemblage of these rocks lacking high amounts of plagioclase. Aegirinization of clinopyroxene-dominated rocks, on the contrary, is obviously blocked by the amount of available ferric iron. This effect thus seems to be the main reason why large-scale aegirinization of submarine mafic alkaline rocks was reported from neither recent nor ancient ocean island complexes.

6. Implications

- Aegirine may occur also in mafic and relatively Na_2O poor alkaline rocks erupted under sea-water or intruded into marine sediments. Its presence then does reflect neither extreme compositional evolution of crystallizing clinopyroxene, nor mixing with a batch of differentiated alkaline melt.

- A compositional gap between the investigated diopside phenocrysts and related aegirine aggregates radiating from these phenocrysts as well as crystallographic discordance suggest that aegirine is not a product of continuous clinopyroxene crystallization in the late magmatic stage. This observation is also supported by the presence of an alteration envelope separating a diopside phenocryst from post-magmatic aegirine.
- Recrystallization of diopside to aegirine in mafic alkaline rocks may represent an alternative process to albitization (spilitization) of MORB-type tholeiitic basalts, but ...
- … the formation of aegirine is controlled and limited by calcium-saturation of seawater (relation to carbonate-compensation depth), and mainly by the amount of available ferric, or oxidizable iron. In highly magnesian rocks, the aegirine will not form on the contact with seawater due to the lack of ferric iron which is not fixed in stable iron oxides (maghemite, magnetite, ulvöspinel).
- The lack of iron necessary for aegirine substitution blocked Na enrichment of the TAR suite, except of the zeolitized essexite TG25 with a low Mg# value of 0.43. In the case of other samples, the linear trend between MgO and Na_2O suggests that sodium for aegirine growth was rather sourced from altered groundmass, and only subordinate amounts of Na could be taken from seawater. This presumption is also confirmed by OIB-normalized trace-element contents.
- The observations from Mesozoic submarine mafic alkaline lavas in the Outer Carpathians explain the absence of spilitization or similar Na-metasomatic processes in submarine mafic alkaline systems worldwide.

Acknowledgements

This work was supported by the Czech Science Foundation project 21-30043S. The manuscript benefitted from constructive comments by reviewers Godfrey Fitton and Axel Renno, as well as by handling editor Chiara Maria Petrone.

References

Ackerman L, Rapprich V, Polák L, Magna T, Mclemore VT, Pour O, Čejková B (2021) Petrogenesis of silica-rich carbonatites from continental rift settings: A missing link between carbonatites and carbonated silicate melts? Journal of Geosciences 66:71-87. http://doi.org/10.3190/jgeosci.320

Banno Y, Yamada S (2012) Sector-zoned aegirine in Sanbagawa quartz schist from the western Kii Peninsula, central Japan. Journal of Mineralogical and Petrological Sciences 107:167-172. https://doi.org/10.2465/jmps.120513

Batki A, Pál-Molnár E, Jankovics MÉ, Kerr AC, Kiss B, Markl G, Heincz A, Harangi S (2018) Insights into the evolution of an alkaline magmatic system: An in situ trace element study of clinopyroxenes from the Ditrău Alkaline Massif, Romania. Lithos 300: 51-71. https://doi.org/10.1016/j.lithos.2017.11.029

Baudouin C, Parat F, Denis CMM, Mangasini F (2016) Nephelinite lavas at early stage of rift initiation (Hanang volcano, North Tanzanian Divergence). Contributions to Mineralogy and Petrology 171:64. https://doi.org/10.1007/s00410-016-1273-5

Baudouin C, France L, Boulanger M, Dalou C, Devidal J-L (2020) Trace element partitioning between clinopyroxene and alkaline magmas: parametrization and role of M1 site on

608 HREE enrichment in clinopyroxenes. Contributions to Mineralogy and Petrology 175:42.
609 https://doi.org/10.1007/s00410-020-01680-6

610 Ben-Yaakov S, Ruth E, Kaplan IR (1974) Carbonate compensation depth: relation to
611 carbonate solubility in ocean waters. Science 184:982-984.
612 https://doi.org/10.1126/science.184.4140.982

613 Breitkreuz C (2013) Spherulites and lithophysae – 200 years of investigation on high-
614 temperature crystallization domains in silica-rich volcanic rocks. Bulletin of Volcanology
615 75:1-16. https://doi.org/10.1007/s00445-013-0705-6

616 Brunarska I, Anczkiewicz R (2019) Geochronology and Sr–Nd–Hf isotope constraints on the
617 petrogenesis of teschenites from the type locality in the Outer Western Carpathians.
618 Geologica Carpathica 70:222-240. https://doi.org/10.2478/geoca-2019-0013

619 Cooper AF, Palin JM, Collins AK (2016) Fenitization of metabasic rocks by ferrocarbonatites
620 at Haast River, New Zealand. Lithos 244:109-121.
621 https://doi.org/10.1016/j.lithos.2015.11.035

622 Chakhmouradian AR, Mitchell RH (2002) The mineralogy of Ba- and Zr-rich alkaline
623 pegmatites from Gordon Butte, Crazy Mountains (Montana, USA): comparisons between
624 potassic and sodic agpaitic pegmatites. Contributions to Mineralogy and Petrology
625 143:93-114. https://doi.org/10.1007/s00410-001-0333-6

626 Decarreau A, Petit S, Vieillard P, Dabert N (2004) Hydrothermal synthesis of aegirine at 200
627 °C. European Journal of Mineralogy 16:85-90. https://doi.org/10.1127/0935-
628 1221/2004/0016-0085

Dempírová L, Šikl J, Kašičková R, Zoulková V, Kříbek B (2010) The evaluation of precision and relative error of the main components of silicate analyses in Central Laboratory of the Czech Geological Survey. Geoscience Research Reports for 2009 43:326-330. (in Czech with English summary)

Dolníček Z, Kropáč K, Uher P, Polách M (2010) Mineralogical and geochemical evidence for multi-stage origin of mineral veins hosted by teschenites at Tichá, Outer Western Carpathians, Czech Republic. Chemie der Erde 70:267-282. https://doi.org/10.1016/j.chemer.2010.03.003

Dostal J, Owen JV (1998) Cretaceous alkaline lamprophyres from northeastern Czech Republic: geochemistry and petrogenesis. Geologische Rundschau 87:67-77. https://doi.org/10.1007/s005310050190

Dunham KC (1933) Crystal cavities in lavas from the Hawaiian Islands. American Mineralogist 18:369-385.

Eby GN, Woolley AR, Din V, Platt G (1998) Geochemistry and petrogenesis of nepheline syenites: Kasungu–Chipala, Ilomba, and Ulindi nepheline syenite intrusions, North Nyasa Alkaline Province, Malawi. Journal of Petrology 39:1405-1424. https://doi.org/10.1093/petrology/39.8.1405

Eliáš M (1979) Facies and paleogeography of the Silesian Unit in the western part of the Czechoslovak Flysch Carpathians. Věstník Ústředního Ústavu Geologického 54:327-339. https://doi.org/10.1190/INT-2020-0109.1

Eliáš M, Skupien P, Vašíček Z (2003) A proposal for the modification of the lithostratigraphical division of the lower part of the Silesian Unit in the Czech area (Outer

651 Western Carpathians). Sborník Vědeckých prací Vysoké Školy báňské, Řada Hornicko-
652 geologická 49:7-13. (in Czech with English summary)

653 Filina MI, Kogarko LN, Kononkova NN (2017) Evolution of pyroxene in peralkaline
654 magmatic system: an example of an agpaitic syenite dyke complex and the Niva
655 intrusion, Kola Peninsula. Geochemistry International 55:663-668.
656 https://doi.org/10.1134/S0016702917070035

657 Flores KE, Skora S, Martin C, Harlow GE, Rodríguez D, Baumgartner PO (2015)
658 Metamorphic history of riebeckite-and aegirine-augite-bearing high-pressure–low-
659 temperature blocks within the Siuna Serpentinite Mélange, northeastern Nicaragua.
660 International Geology Review 57:943-977.
661 https://doi.org/10.1080/00206814.2015.1027747

662 Fortey NJ, Michie,UMcL (1978) Aegirine of possible authigenic origin in Middle Devonian
663 sediments in Caithness, Scotland. Mineralogical Magazine 42:439-442.
664 https://doi.org/10.1180/minmag.1978.042.324.05

665 Galliski MA, Lira R, Dorais MJ (2004) Low-pressure differentiation of melanephelinitic
666 magma and the origin of ijolite pegmatites at La Madera, Córdoba, Argentina. The
667 Canadian Mineralogist 42:1799-1823. https://doi.org/10.2113/gscanmin.42.6.1799

668 Ghose NC, Singh AK, Dutt A, Imtisunep S (2021) Significance of aegirine-bearing metabasic
669 rocks in the metamorphic evolution of the Nagaland Accretionary Prism, northeast India.
670 Geological Journal. https://doi.org/10.1002/gj.4317

671 Haloda J, Rapprich V, Holub FV, Halodová P, Vaculovič T (2010) Crystallization history of
672 Oligocene ijolitic rocks from the Doupovské hory Volcanic Complex (Czech Republic).
673 Journal of Geosciences 55:279-297. http://doi.org/10.3190/jgeosci.076

674 Hyndman DW (1972) Petrology of Igneous and Metamorphic Rocks. McGraw-Hill, New
675 York.

676 Janoušek V, Farrow CM, Erban V (2006) Interpretation of whole-rock geochemical data in
677 igneous geochemistry: introducing Geochemical Data Toolkit (GCDkit). Journal of
678 Petrology 47:1255-1259. http://doi.org/10.1093/petrology/egl013

679 Jochum KP, Nohl U, Herwig K, Lammel E, Stoll B, Hofmann AW (2005) GeoReM: A New
680 Geochemical Database for Reference Materials and Isotopic Standards. Geostandards and
681 Geoanalytical Research 29:333-338. https://doi.org/10.1111/j.1751-908X.2005.tb00904.x

682 Jochum KP, Weis U, Stoll B, Kuzmin D, Yang Q, Raczek I, Jacob DE, Stracke A, Birbaum
683 K, Frick DA, Günther D, Enzweiler J (2011) Determination of reference values for NIST
684 SRM 610–617 glasses following ISO guidelines. Geostandards and Geoanalytical
685 Research 35:397-429. https://doi.org/10.1111/j.1751-908X.2011.00120.x

686 Johnson SY, Alam AMN (1991) Sedimentation and tectonics of the Sylhet trough,
687 Bangladesh. Geological Society of America Bulletin 103:1513-1527.
688 https://doi.org/10.1130/0016-7606(1991)103<1513:SATOTS>2.3.CO;2

689 Kropáč K, Dolníček Z, Uher P, Urubek T (2017) Fluorcaphite from hydrothermally altered
690 teschenite at Tichá, Outer Western Carpathians, Czech Republic: compositional
691 variations and origin. Mineralogical Magazine 81:1485-1501.
692 https://doi.org/10.1180/minmag.2017.081.016

693 Kropáč K, Dolníček Z, Uher P, Buriánek D, Safai A, Urubek T (2020) Zirconian–niobian
694 titanite and associated Zr-, Nb-, REE-rich accessory minerals: Products of hydrothermal
695 overprint of leucocratic teschenites (Silesian Unit, Outer Western Carpathians, Czech
696 Republic). Geologica Carpathica 71:343-360. https://doi.org/10.31577/GeolCarp.71.4.4

697 Larsen LM (1976) Clinopyroxenes and coexisting mafic minerals from the alkaline
698 Ilímaussaq intrusion, South Greenland. Journal of Petrology 17:258-290.
699 https://doi.org/10.1093/petrology/17.2.258

700 Le Maitre RW (ed), Streckeisen A, Zanettin B, Le Bas MJ, Bonin B, Bateman P, Bellieni G,
701 Dudek A, Efremova S, Keller J, Lameyre J, Sabine PA, Schmid R, Sørensen H, Wooley
702 AR (2002) Igneous rocks. A classification and glossary of terms. Recommendations of
703 the International Union of Geological Sciences Subcommission on the Systematics of
704 Igneous Rocks, 2nd edn. Cambridge University Press, Cambridge-New York.

705 Li Y, Pu R, Zhang G, Qu H (2021) Characteristics and origins of ridges and troughs on the
706 top of the Middle Miocene strata in the Beijiao Sag of the Qiongdongnan Basin, northern
707 South China Sea. Interpretations 9:SB1-SB15. https://doi.org/10.1190/INT-2020-0109.1

708 Lucińska-Anczkiewicz A, Villa IM, Anczkiewicz R, Slaczka A (2002) $^{40}Ar/^{39}Ar$ dating of
709 alkaline lamprophyres from the Polish Western Carpathians. Geologica Carpathica 53:45-
710 52.

711 Machek P, Matýsek D (1994) Mathematical-statistical study of chemical composition of the
712 teschenite association rocks. Sborník Geologických Věd - Geologie 46, 125-141.

713 Mann U, Marks M, Markl G (2006) Influence of oxygen fugacity on mineral compositions in
714 peralkaline melts: The Katzenbuckel volcano, Southwest Germany. Lithos 91:262-285.
715 https://doi.org/10.1016/j.lithos.2005.09.004

716 Markl G, Marks MA, Frost BR (2010) On the controls of oxygen fugacity in the generation
717 and crystallization of peralkaline melts. Journal of Petrology 51:1831-1847.
718 https://doi.org/10.1093/petrology/egq040

719 Matýsek D (1992) Statistical evaluation of the chemical composition of pyroxenes and
720 amphiboles of the teschenite association. Časopis pro Mineralogii a Geologii 37:89-96.

721 Matýsek D, Jirásek J (2016) Occurrences of slawsonite in rocks of the Teschenite Association
722 in the Podbeskydí Piedmont Area (Czech Republic) and their petrological significance.
723 Canadian Mineralogist 54:1129-1146. https://doi.org/10.3749/canmin.1500101

724 McSween HY, Eisenhour DD, Taylor LA, Wadhwa M, Crozaz G (1996) QUE94201
725 shergottite: crystallization of a Martian basaltic magma. Geochimica et Cosmochimica
726 Acta 60:4563-4569. https://doi.org/10.1016/S0016-7037(96)00265-7

727 McSwiggen PL, Morey GB, Cleland JM (1994) The origin of aegirine in iron formation of the
728 Cuyuna Range, east-central Minnesota. Canadian Mineralogist 32:589-598.

729 Menčík E, Adamová M, Dvořák J, Dudek A, Jetel J, Jurková A, Hanzlíková E, Houša V,
730 Peslová H, Rybářová L, Šmíd B, Šebesta J, Tyráček J, Vašíček Z (1983) Geology of the
731 Moravskoslezské Beskydy Mts. andthe Podbeskydská pahorkatina Upland. Academia,
732 Praha. (in Czech with English summary)

733 Monecke T, Renno AD, Herzig PM (2004) Primary clinopyroxene spherulites in basaltic
734 lavas from the Pacific–Antarctic Ridge. Journal of Volcanology and Geothermal
735 Research 130:51-59. https://doi.org/10.1016/S0377-0273(03)00278-6

736 Morimoto N, Fabries J, Ferguson AK, Ginzburg IV, Ross M, Seifert FA, Zussman J, Aoki K,
737 Gottardi G (1988) Nomenclature of pyroxenes. Mineralogy and Petrology 39:55-76.
738 https://doi.org/10.1007/BF01226262

739 Pacák O (1926) Sopečné horniny na severním úpatí Bezkyd Moravských. Česká matice věd a
740 umění, Praha. (in Czech)

741 Palme H, Lodders K, Jones A (2014) Solar system abundances of the elements. In Davis AM
742 (ed.): Planets, Asteriods, Comets and The Solar System, Volume 2 of Treatise on
743 Geochemistry (Second Edition). Elsevier, pp. 15–36. http://dx.doi.org/10.1016/B978-0-
744 08-095975-7.00118-2

745 Paton C, Hellstrom J, Paul B, Woodhead J, Hergt J (2011) Iolite: Freeware for the
746 visualisation and processing of mass spectrometric data. Journal of Analytical Atomic
747 Spectrometry. doi:10.1039/c1ja10172b.

748 Pazdernik P (1997) Phonolitic and trachytic rocks in the České Středohoří Mts., North
749 Bohemia: geochemistry and petrology. Journal of the Czech Geological Society 42: 68.

750 Pearce JA (1996) A user's guide to basalt discrimination diagrams. In: Wyman DA (ed):
751 Trace element geochemistry of volcanic rocks: applications for massive sulphide
752 exploration. Geological Association of Canada, Short Course Notes 12, pp 79-113.

753 Picha FJ, Stráník Z, Krejčí O (2006) Geology and hydrocarbon resources of the Outer
754 Western Carpathians and their foreland, Czech Republic. In: Golonka J, Picha J (eds:The

Carpathians and their foreland: geology and hydrocarbon resources. AAPGMemoir 84, Tulsa, pp 49-175. https://doi.org/10.1306/985607M843067

Piilonen PC, McDonald AM, Lalonde AE (1998) The crystal chemistry of aegirine from Mont Saint-Hilaire, Quebec. Canadian Mineralogist 36:779-791.

Pour O, Rapprich V, Matýsek D, Jirásek J (2022) About the origin of analcime in Meso- and Cenozoic volcanic rocks of the Czech Republic and its role in rock classification. Geoscience Research Reports 55:75-81. https://doi.org/10.3140/zpravy.geol.2022.10

Rapprich V (2005) Compositional variation of clinopyroxenes of basaltic, essexitic and tephriphonolitic rocks from the Doupovské hory Volcanic Complex, NW Bohemia. Journal of Geosciences 50:119-132. https://doi.org/10.3190/jcgs.982

Redhammer GJ, Tippelt G, Amthauer G, Roth G (2012) Structural and ^{57}Fe Mössbauer spectroscopic characterization of the synthetic $NaFeSi_2O_6$ (aegirine) – $CaMgSi_2O_6$ (diopside) solid solution series. Zeitschrift für Kristallographie 227:396-410. https://doi.org/10.1524/zkri.2012.1514

Redhammer GJ, Weber J, Tippelt G, Zickler GA, Reyer A (2019) Low temperature synthesis of aegirine $NaFeSi_2O_6$: spectroscopy (^{57}Fe Mössbauer, Raman) and size/strain analysis from X-ray powder difraction. Minerals 9:444; https://doi.org/10.3390/min9070444

Rosenbauer RJ, Bischoff JL, Zierenberg RA (1988) The laboratory albitization of mid-ocean ridge basalt. The Journal of Geology 96:237-244. https://doi.org/10.1086/629213

Schmid SM, Bernoulli D, Fügenschuh B, Matenco L, Schefer S, Schuster R, Tischler M, Ustaszewski K (2008) The alpine-Carpathian-Dinaridic orogenic system - correlation and

776 evolution of tectonic units. Swiss Journal of Geosciences 101:139-183.
777 https://doi.org/10.1007/s00015-008-1247-3

778 Shearer CK, Larsen LM (1994) Sector-zoned aegirine from the Ilímaussaq alkaline intrusion,
779 South Greenland: Implications for trace-element behavior in pyroxene. American
780 Mineralogist 79:340-352.

781 Šmíd B (1978) Výzkum vyvřelých hornin těšínitové asociace. Unpublished dissertation.
782 Ústřední ústav geologický. (in Czech)

783 Sun SS, McDonough WF (1989) Chemical and isotopic systematics of oceanic basalts:
784 implications for mantle composition and processes. Geological Society London, Special
785 Publication 42:313–345. https://doi.org/10.1144/GSL.SP.1989.042.01.19

786 Sutherland DS (1969) Sodic amphiboles and pyroxenes from fenites in East Africa. Contrib
787 Mineral Petr 24:114-135. https://doi.org/10.1007/BF00376886

788 Szopa K, Włodyka R, Chew D (2014) LA-ICP-MS U-Pb apatite dating of Lower Cretaceous
789 rocks from teschenite-picrite association in the Silesian Unit (southern Poland).
790 Geologica Carpathica 65:273-284. https://doi.org/10.2478/geoca-2014-0018

791 Tracy RJ, Robinson P (1977) Zoned titanian augite in alkali olivine basalt from Tahiti and
792 nature of titanian substitutions in augite. American Mineralogist 62:634–645.

793 Ulrych J, Povondra P, Pivec E, Rutšek J, Bendl J, Bilik I (1996) Alkaline ultramafic sill at
794 Dvůr Králové nad Labem, eastern Bohemia: petrological and geochemical constraints.
795 Acta Universitatis Carolinae, Geologica 40:53-79.

796 Vatin-Perignon N, Shaw D M, Muysson JR (1979) Abundance of lithium in spilites and its
797 implications for the spilitization process. Physics and Chemistry of the Earth 11:465-478.
798 https://doi.org/10.1016/0079-1946(79)90044-2

799 Vieten K, Hamm HM (1978) Additional notes "On the calculation of the crystal chemical
800 formula of clinopyroxenes and their contents of Fe^{3+} from microprobe analyses". Neues
801 Jahrbuch für Mineralogie, Monatshefte 2:71-83.

802 Weidendorfer D, Schmidt MW, Mattsson HB (2016) Fractional crystallization of Si-
803 undersaturated alkaline magmas leading to unmixing of carbonatites on Brava Island
804 (Cape Verde) and a general model of carbonatite genesis in alkaline magma suites.
805 Contributions to Mineralogy and Petrology 171:43. https://doi.org/10.1007/s00410-016-
806 1249-5

807 Włodyka R (2010) The evolution of mineral composition of the Cieszyn magma province
808 rocks. Wydawnictwo Uniwersytetu Śląskiego. Katowice. (in Polish with English
809 summary)

810 Woolley AR, Williams CT, Wall F, Garcia D, Moute J (1995) The Bingo carbonatite-ijolite-
811 nepheline syenite complex, Zaire: geology, petrography, mineralogy and petrochemistry.
812 Journal of African Earth Sciences 21:329-348. https://doi.org/10.1016/0899-
813 5362(95)00093-9

814 Yagi K (1966) The system acmite-diopside and its bearing on the stability relations of natural
815 pyroxenes of the acmite-hedenbergite-diopside series. American Mineralogist 51:976-
816 1000.

817 Yoshikawa K (1977) Phase relations and the nature of clinopyroxene solid solution in the
818 system $NaFe^{3+}Si_2O_6$ - $CaMgSi_2O_6$ - $CaAl_2SiO_6$. Journal of the Faculty of Science,
819 Hokkaido University. Series 4, Geology and mineralogy, 17:451-485.

820

821 **Figure captions**

822 **Fig. 1.** Schematic geological map of the occurrences of the teschenite association rocks
823 (TAR) in the Czech part of the Podbeskydí area with the positions of the studied localities
824 (adapted after Matýsek and Jirásek 2016). Notes: 1) contacts between the Subsilesian,
825 Silesian, and Magura units are always tectonic (thrusts), the uncertain facies most likely
826 represent incomplete erosional remnants of the Godula and Kelč facies, 2) Pouzdřany unit and
827 Ždánice part of the Ždánice-Subsilesian units does not occur in depicted area. Foremagura
828 unit is in the given area represented by generally small tectonic slices, which were
829 intentionally omitted from the picture (they are off interest of this article).

830 **Fig. 2.** BSE images of aegirine and aegirine-augite forms and accompanying minerals from
831 the TAR localities: **a –** aegirine needles enclosed in natrolite (etched in diluted acetic acid),
832 Jasenice village (49.5301°N, 17.9616°E); **b –** aegirine accompanied by laths of partially
833 albitized K-feldspar and natrolite, Lubno (49.6025°N, 18.3634°E); **c –** radial spray of aegirine
834 needles integrown with mineral of the pyrochlore group, Hradiště (49.7356°N, E 18.5250°E);
835 **d –** aegirine post-dating crystallization of fluorcarphite on apatite, all enclosed in natrolite,
836 Borošín (TG25 in tab. 1); **e –** euhedral and compositionally zoned aegirine to aegirine-augite
837 showing rather uncommon decrease of aegirine component towards rim, Krmelín (49.7226°N,
838 18.2449°E); **f –** miarolic cavity with euhedral aegirine crystals on K-feldspar and analcime,
839 Borošín (TG25 in Tab. 1). Mineral symbols: Aeg – aegirine, Aeg-Aug – aegirine-augite, Ap –
840 apatite, Fcp – fluorcaphite, FSp – feldspar group minerals, Ntr – natrolite, Pcl – Pyrochlore.

Fig. 3. Microphotographs of the studied rocks containing aegirine suitable for analytical work: **a –** aegirine at the tip of larger, partly altered diopside phenocryst in devitrified porphyritic amphibole-bearing augitite from Petřkovická hora (TG05); **b –** aegirine growing from partly altered diopside phenocryst in analcimized essexite from Stříbrník (TG13); **c,d –** aegirine growing from partly altered diopside phenocryst in analcimized phoscoritic ijolite from Tichá (TG15); **e –** aegirine growing from partly altered diopside phenocryst in analcimized ijolite from Tichá (TG22), note the slight rotation of the aegirine c-axis compared to diopside phenosryst; **f –** euhedral aegirine on diopside phenocryst and in the groundmass in natrolitized essexite from Borošín (TG25); **g –** aegirine radial spray enclosed in natrolite in natrolitized essexite from Borošín (TG25); **h –** aegirine coating on diopside and amphibole in camptonite from Perná (TG37). Aeg – aegirine, Amp – amphibole, Anl – analcime, Ant – anatase, Ap – apatite, Bt – biotite, Cal – calcite, Di – diopside, gm – groundmass, Mag – magnetite, Mgh – maghemite, Ntr – natrolite, s – spherulitically devitrified glass, Sd – siderite, Ttn – titanite, red arrows indicate alteration zones separating primary diopside from secondary aegirine.

Fig. 4. Back-scattered electron (BSE) images of the studied rocks: **a –** radial spray and euhedral grains of aegirine in zeolitized augitite TG05, note the completely altered diopside phenocryst, on which a fresh aegirine crystallized; **b –** aegirine in groundmass and attached to diopside phenocryst in zeolitized (analcime) essexite TG13. Note the radial aggregates of feldspars surrounded by analcime, a possible result of glass devitrification; **c,d –** radial sprays of aegirine in zeolitized (natrolite) essexite TG25 (c – natural fracture surface, d – polished surface); **e,f –** sector- and growth-zoned diopside coated with hedenbergite, and with attached aegirine crystals from camptonite TG37. Aeg – aegirine, Ap – apatite, Anl – analcime, Cal – calcite, Di – diopside, ex-Di – altered diopside, Fsp – feldpsars, Hd – hedenbergite, Ntr –

865 natrolite, white arrows indicate alteration zones separating primary diopside from secondary
866 aegirine.

867 **Fig. 5.** Chemical composition of the studied rocks: **a –** TAS classification diagram (Le Maitre
868 et al. 2002), names of intrusive equivalents added, m.g. – monzo-gabbro, t.b. – trachy-basalt;
869 **b –** Zr/Ti vs. Nb/Y classification diagram of volcanic rocks (Pearce 1996), names of the
870 intrusive equivalents added; **c –** Na_2O vs. MgO binary diagram, note the samples dropping
871 below the general differentiation trend, suggesting post-magmatic loss of Na due to
872 weathering/alteration.

873 **Fig. 6.** The studied pyroxenes in the classification diagrams (Morimoto 1988): **a –** sodic vs.
874 quadrilateral pyroxenes (Jd-Quad-Ae ternary diagram); **b –** quadrilateral diagram (En-Wo-Fs
875 ternary diagram), the aegirine and aegirine-augite dots are plotted only in half-tones to show
876 the trend, but these analyses should not be classified in the quadrilateral diagram.

877 **Fig. 7.** Distribution maps of selected major elements in the sample TG37 displaying the
878 compositional contrasts between a diopside phenocryst, its hedenbergite to aegirine-augite rim
879 and the attached aegirine crystal.

880 **Fig. 8.** Spider-grams of incompatible trace elements: **a –** chondrite (Palme et al. 2014) -
881 normalized REE patterns; **b –** ocean-island basalt (OIB: Sun and McDonough 1989) –
882 normalized patterns of the extended trace element contents, the Rb content of the primary
883 diopsides is mostly plotted below the 0.001 line.

884 **Fig. 9.** Simplified sketch model for the origin of aegirine from reaction of (ultra)mafic
885 alkaline rock with seawater: **a –** original diopside phenocryst enclosed in nephelinic/glassy
886 groundmass; **b –** alteration of diopside and devitrification/zeolitization of groundmass; **c –**
887 growth of secondary aegirine with Fe^{3+} sourced from altered diopside and Na sourced from
888 groundmass.

Tables

Table 1. Overview of the sampled localities, rock types and their mineral composition based on quantitative X-ray diffraction analyses (primary phases in bold).

Electronic Supplementary Material

ESM1. Bulk-rock composition of TAR. Major oxides in wt%, trace elements in ppm.

ESM2. Clinopyroxene mineral chemistry data: major oxides in wt%, crystal-chemical formulae in *apfu* (atoms per formula unit), trace elements in ppm.

Table 1. Overview of the sampled localities, rock types and their mineral composition based on quantitative X-ray diffraction analyses (primary phases in bold).

Sample	Locality	coordinates	rock type	**rock composition** in wt% (primary phases in bold)
TG05	Petřkovická hora near Starý Jičín	49.54262°N 17.95967°E	Devitrified amphibole-bearing augitite	17% microcline, 17% analcime, 16% albite, **15% Fe-diopside**, 11% chlorite, 9% calcite, **8% amphibole**, **4% apatite**, 2% quartz, **1% biotite**
TG13	Stříbrník near Ostravice	49.53413°N 18.36862°E	Zeolitized (analcime) essexite	30% analcime, **21% Fe-diopside**, 18% microcline, 13% chlorite, 6% albite, **5% biotite**, **3% apatite**, 3% anatase, **1% amphibole**
TG15	Tichá – gorge of unnamed left-bank tributary to Tichávka creek	49.56983°N 18.22672°E	Phoscoritic ijolite (analcimized)	**18% apatite, 18% phlogopite, 18% amphibole**, 10% chlorite, 8% plagioclase, **7% diopside**, 5% siderite, **5% maghemite,** 5% analcime, 4% calcite, 2% anatase
TG22	Tichá – Tichávka creek gorge, under the church	49.57095°N 18.22385°E	Zeolitized (analcime) ijolite	33% analcime, 16% chlorite, 15% albite, 11% calcite, 6% microcline, **6% Fe-diopside**, 6 % quartz, 4% anatase**, 2% apatite**, **1% amphibole**, **1% biotite**
TG25	Borošín	49.69207°N 18.23897°E	Zeolitized (natrolite) essexite	50% natrolite, **22% Fe-diopside**, 8 % orthoclase, 5% kaolinite, **5% aegirne**, **4% annite**, 4% chlorite, **2% apatite**
TG37	unnamed hill 374 m a.s.l. near Perná	49.53370°N 17.95067°E	Camptonite	34% analcime, **19% amphibole**, 15% microcline, **14% plagioclase**, **14% Fe-diopside**, **3% apatite**, 1% chlorite

Figure 1

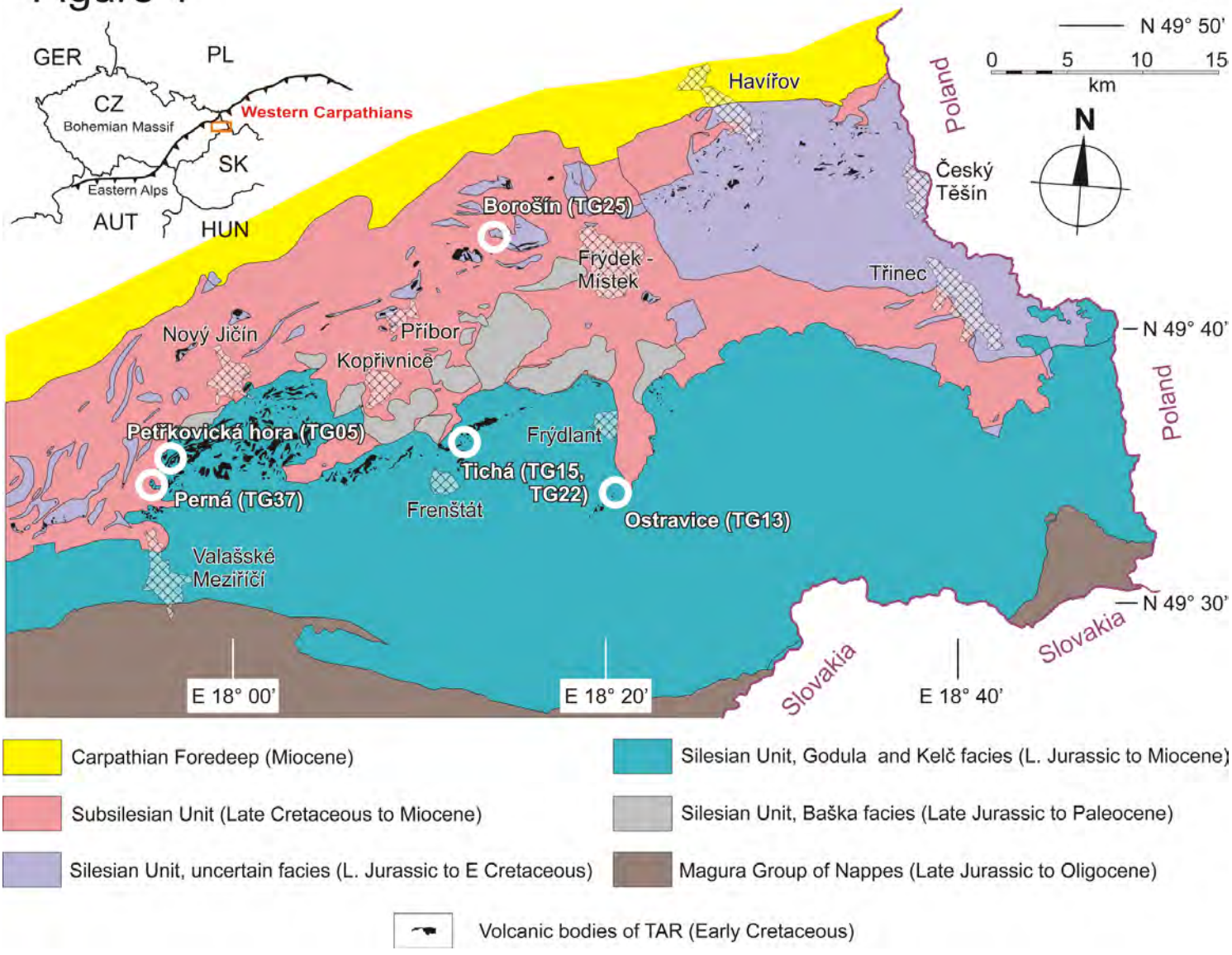

Carpathian Foredeep (Miocene)

Subsilesian Unit (Late Cretaceous to Miocene)

Silesian Unit, uncertain facies (L. Jurassic to E Cretaceous)

Silesian Unit, Godula and Kelč facies (L. Jurassic to Miocene)

Silesian Unit, Baška facies (Late Jurassic to Paleocene)

Magura Group of Nappes (Late Jurassic to Oligocene)

Volcanic bodies of TAR (Early Cretaceous)

Fig. 2

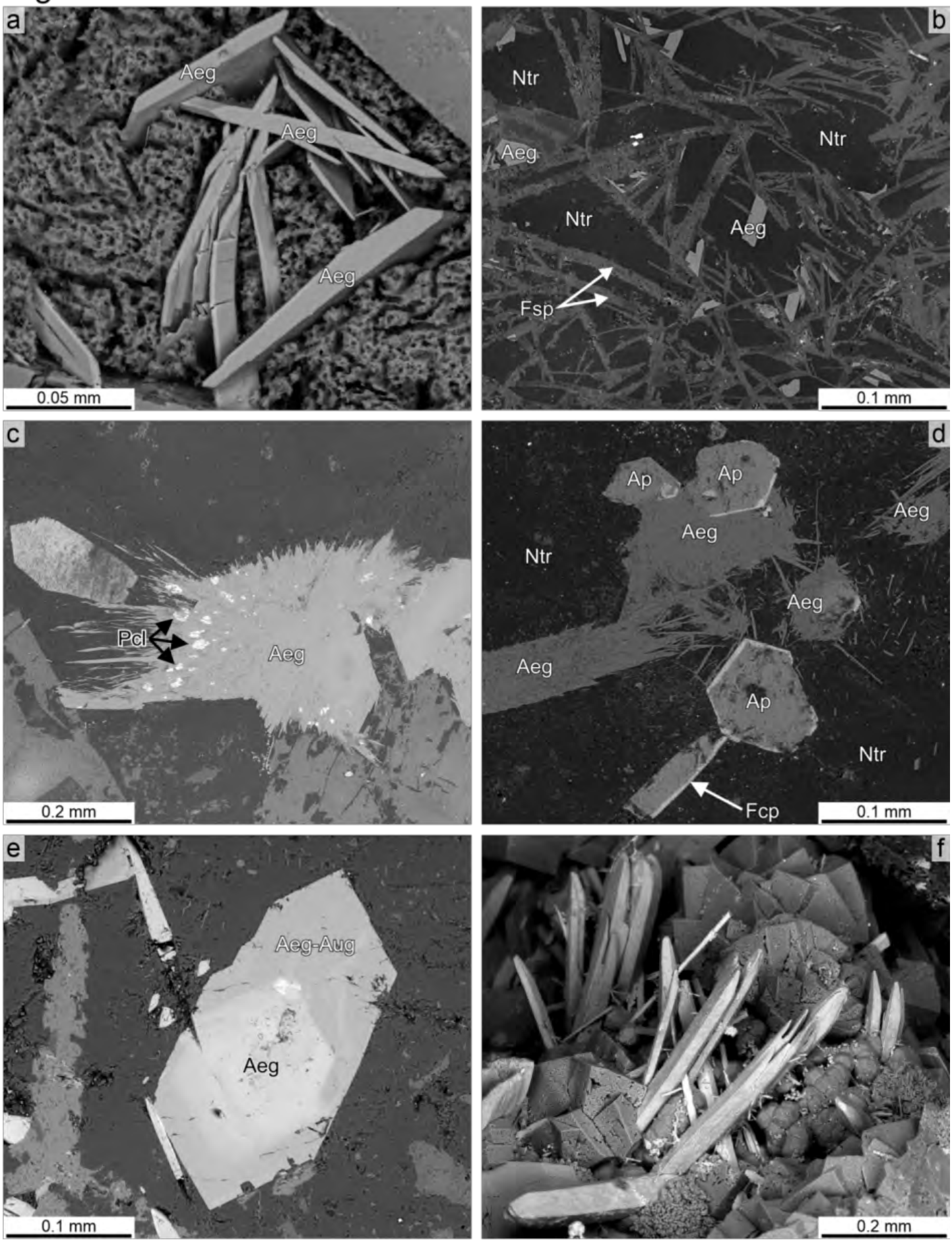
a
Aeg
Aeg
Aeg
0.05 mm
b
Ntr
Ntr
Aeg
Ntr
Aeg
Fsp
0.1 mm
c
Pcl
Aeg
0.2 mm
d
Ap
Ap
Aeg
Aeg
Ntr
Aeg
Aeg
Ap
Ntr
Fcp
0.1 mm
e
Aeg-Aug
Aeg
0.1 mm
f
0.2 mm

Fig. 3

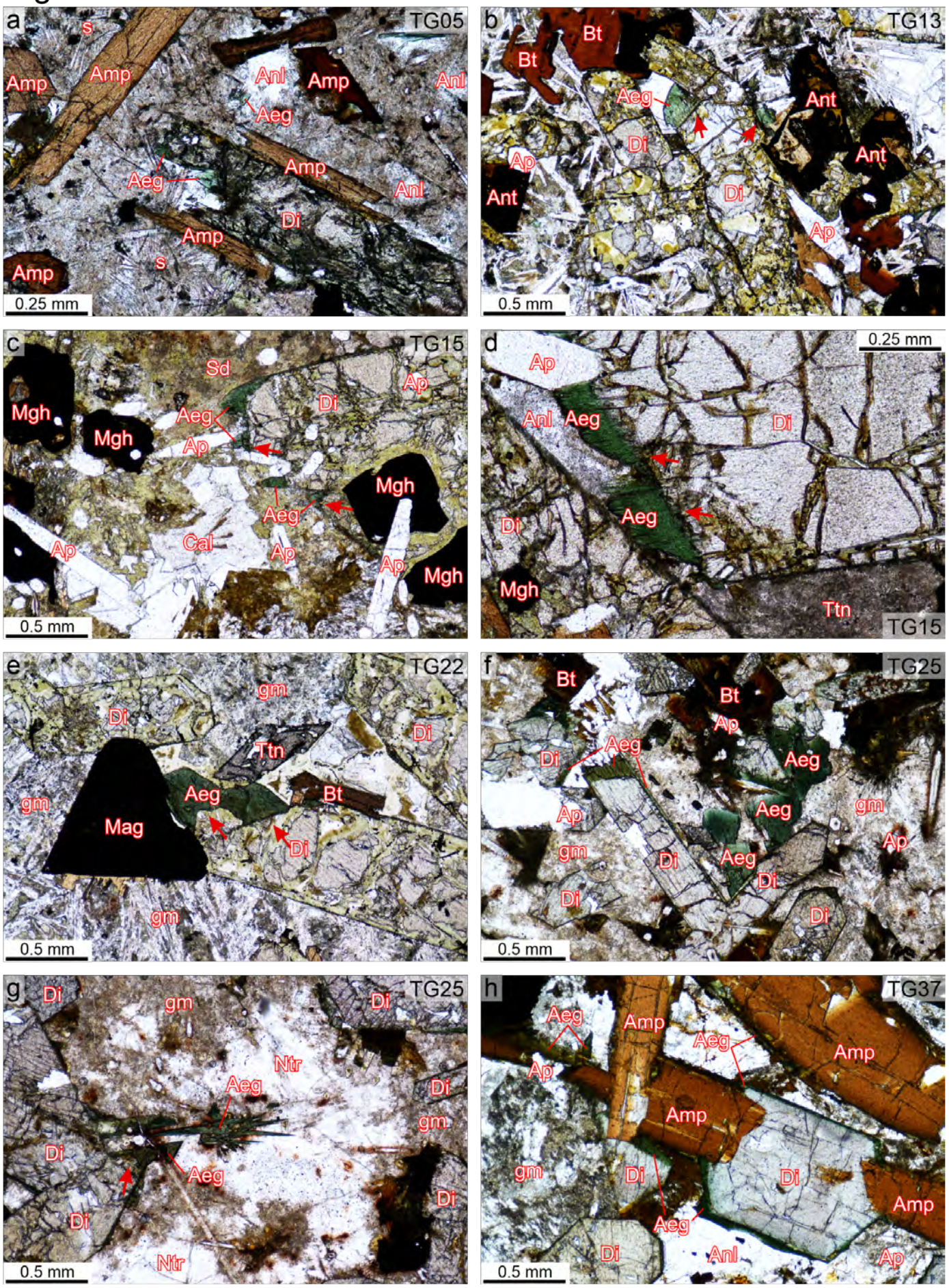
a
TG05
s
Amp
Amp
Anl
Amp
Anl
Aeg
Amp
Aeg
Anl
Di
Amp
Amp
s
0.25 mm
b
TG13
Bt
Bt
Aeg
Ant
Di
Ant
Ap
Ant
Di
Ap
0.5 mm
c
TG15
Sd
Ap
Mgh
Di
Aeg
Mgh
Ap
Mgh
Aeg
Ap
Cal
Ap
Ap
Mgh
0.5 mm
d
0.25 mm
Ap
Anl
Aeg
Di
Aeg
Di
Mgh
Ttn
TG15
e
TG22
gm
Di
Di
Ttn
Aeg
Bt
gm
Mag
Di
gm
0.5 mm
f
TG25
Bt
Bt
Ap
Aeg
Di
Aeg
Aeg
gm
Ap
Ap
gm
Di
Aeg
Di
Di
Di
0.5 mm
g
Di
gm
TG25
Di
Ntr
Aeg
Di
gm
Di
Aeg
Di
Di
Ntr
0.5 mm
h
TG37
Aeg
Amp
Aeg
Amp
Ap
Amp
gm
Di
Di
Amp
Aeg
Di
Anl
Ap
0.5 mm

Fig. 4

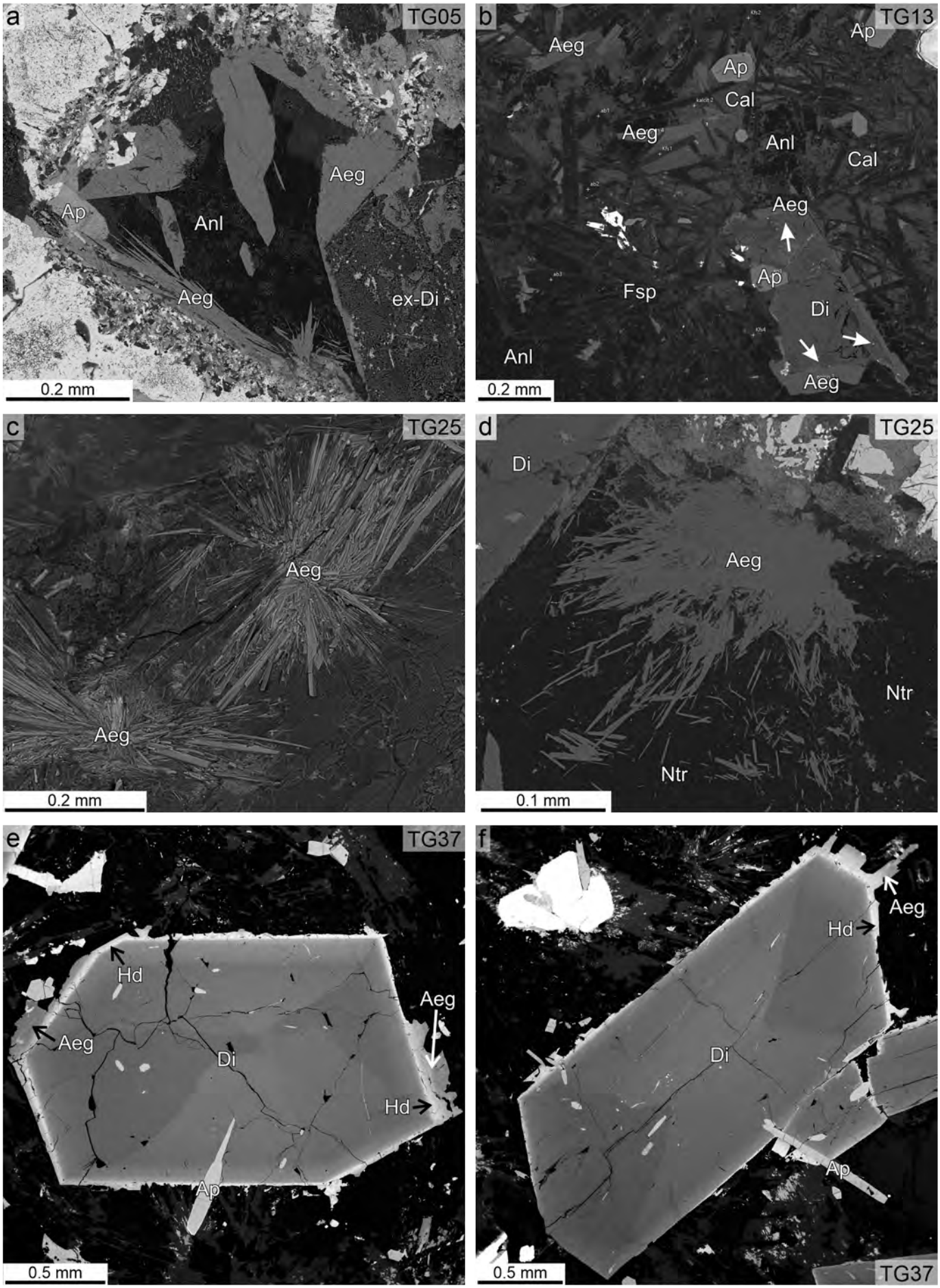
a
TG05
Aeg
Ap
Anl
Aeg
Aeg
ex-Di
0.2 mm
b
TG13
Aeg
Ap
Ap
Cal
Aeg
Anl
Cal
Aeg
Ap
Fsp
Di
Anl
Aeg
0.2 mm
c
TG25
Aeg
Aeg
0.2 mm
d
TG25
Di
Aeg
Ntr
Ntr
0.1 mm
e
TG37
Hd
Aeg
Aeg
Di
Hd
Ap
0.5 mm
f
Aeg
Hd
Di
Ap
0.5 mm
TG37

Fig. 5

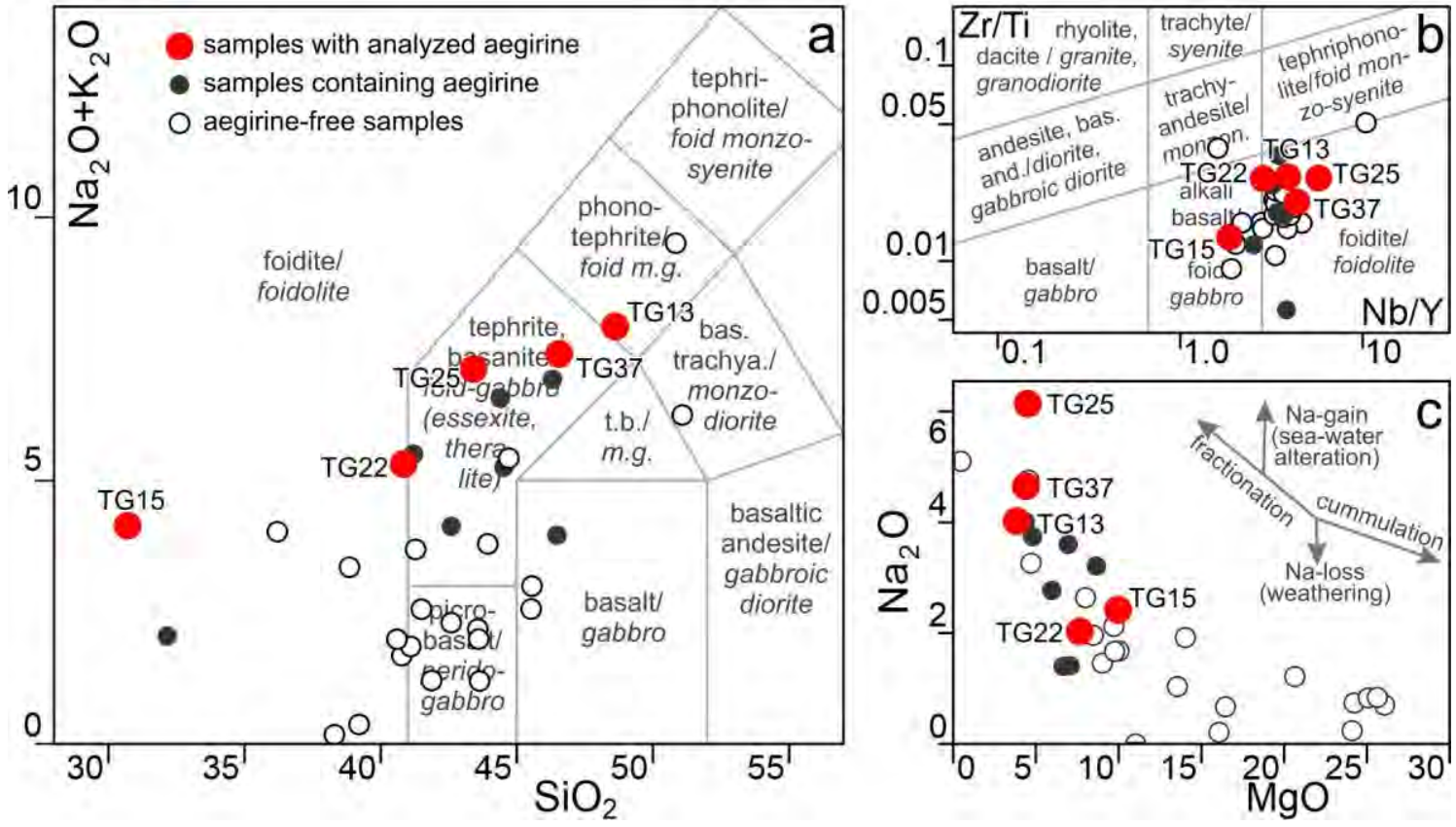
samples with analyzed aegirine
samples containing aegirine
aegirine-free samples
a
Na2O+K2O
SiO2
foidite/ foidolite
tephri-phonolite/ foid monzo-syenite
phono-tephrite/ foid m.g.
tephrite, basanite foid-gabbro (essexite, thera-lite)
bas. trachya./ monzo-diorite
t.b./ m.g.
basaltic andesite/ gabbroic diorite
basalt/ gabbro
picro-basalt/ perido-gabbro
TG13
TG25
TG37
TG22
TG15
b
Zr/Ti
Nb/Y
rhyolite, dacite / granite, granodiorite
trachyte/ syenite
tephriphono-lite/foid mon-zo-syenite
andesite, bas. and./diorite, gabbroic diorite
trachy-andesite/ mon.
alkali basalt
foidite/ foidolite
basalt/ gabbro
foid gabbro
c
Na2O
MgO
Na-gain (sea-water alteration)
fractionation
cummulation
Na-loss (weathering)

Fig. 6

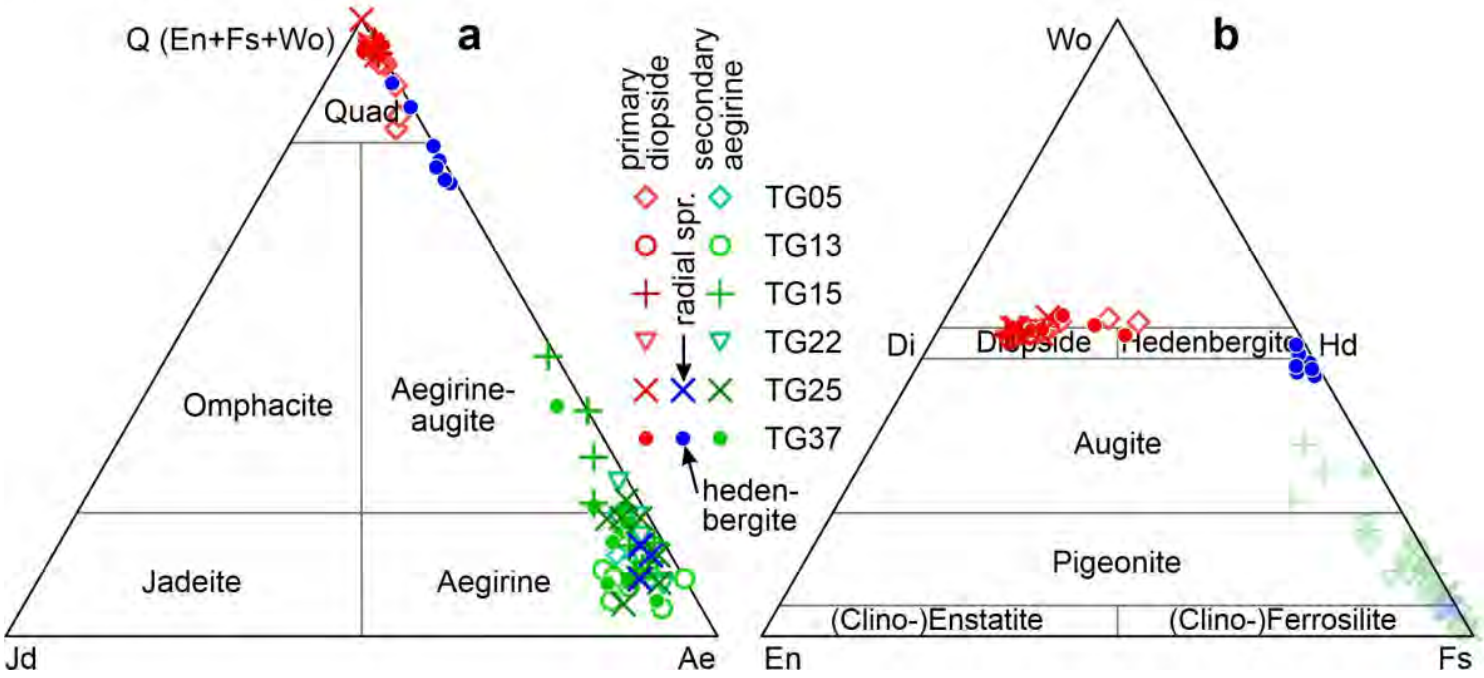
Q (En+Fs+Wo)
a
Quad
Omphacite
Aegirine-
augite
Jadeite
Aegirine
Jd
Ae
primary
diopside
secondary
aegirine
radial spr.
TG05
TG13
TG15
TG22
TG25
TG37
heden-
bergite
Wo
b
Di
Diopside
Hedenbergite
Hd
Augite
Pigeonite
(Clino-)Enstatite
(Clino-)Ferrosilite
En
Fs

Fig. 7

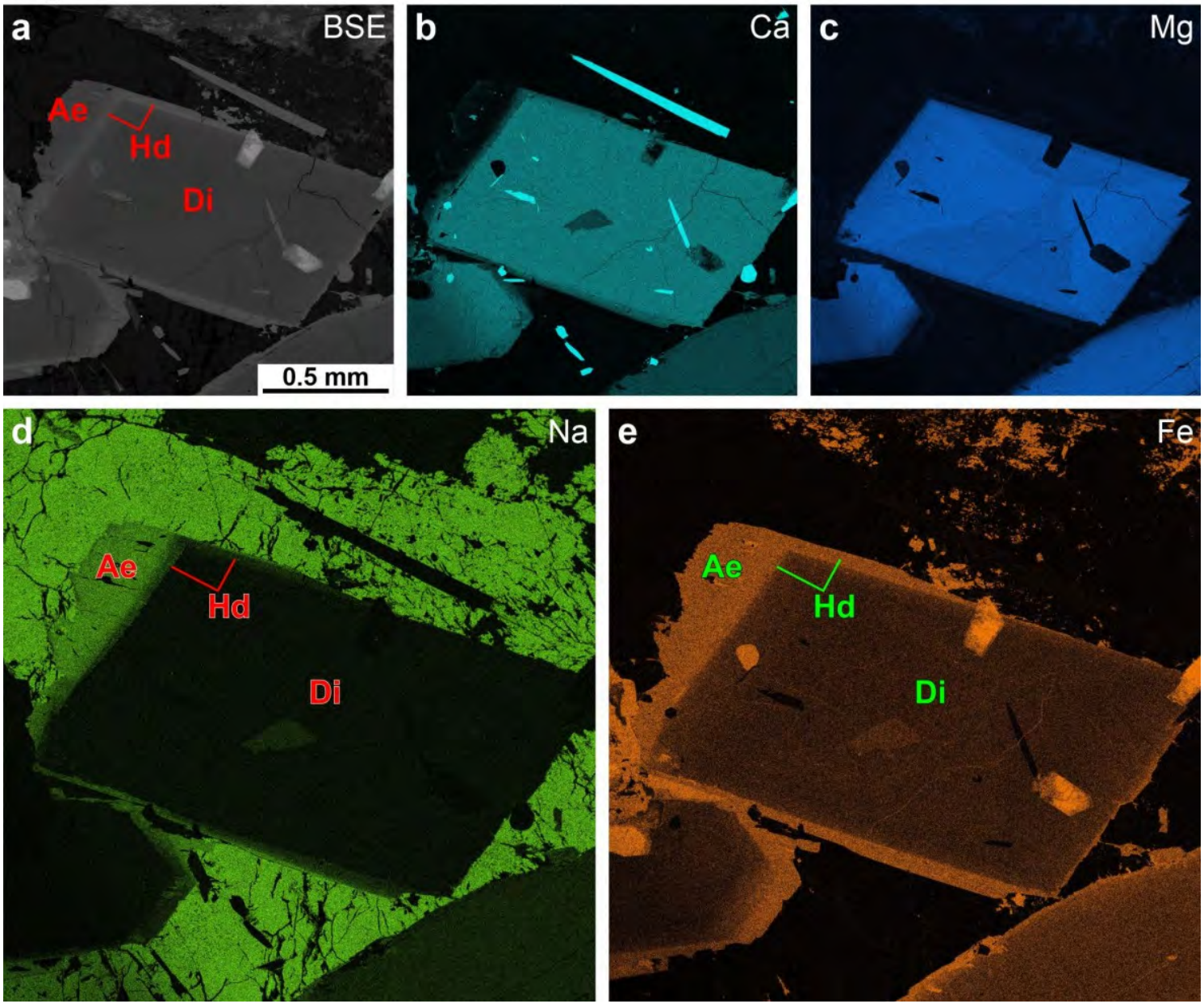

Fig. 8

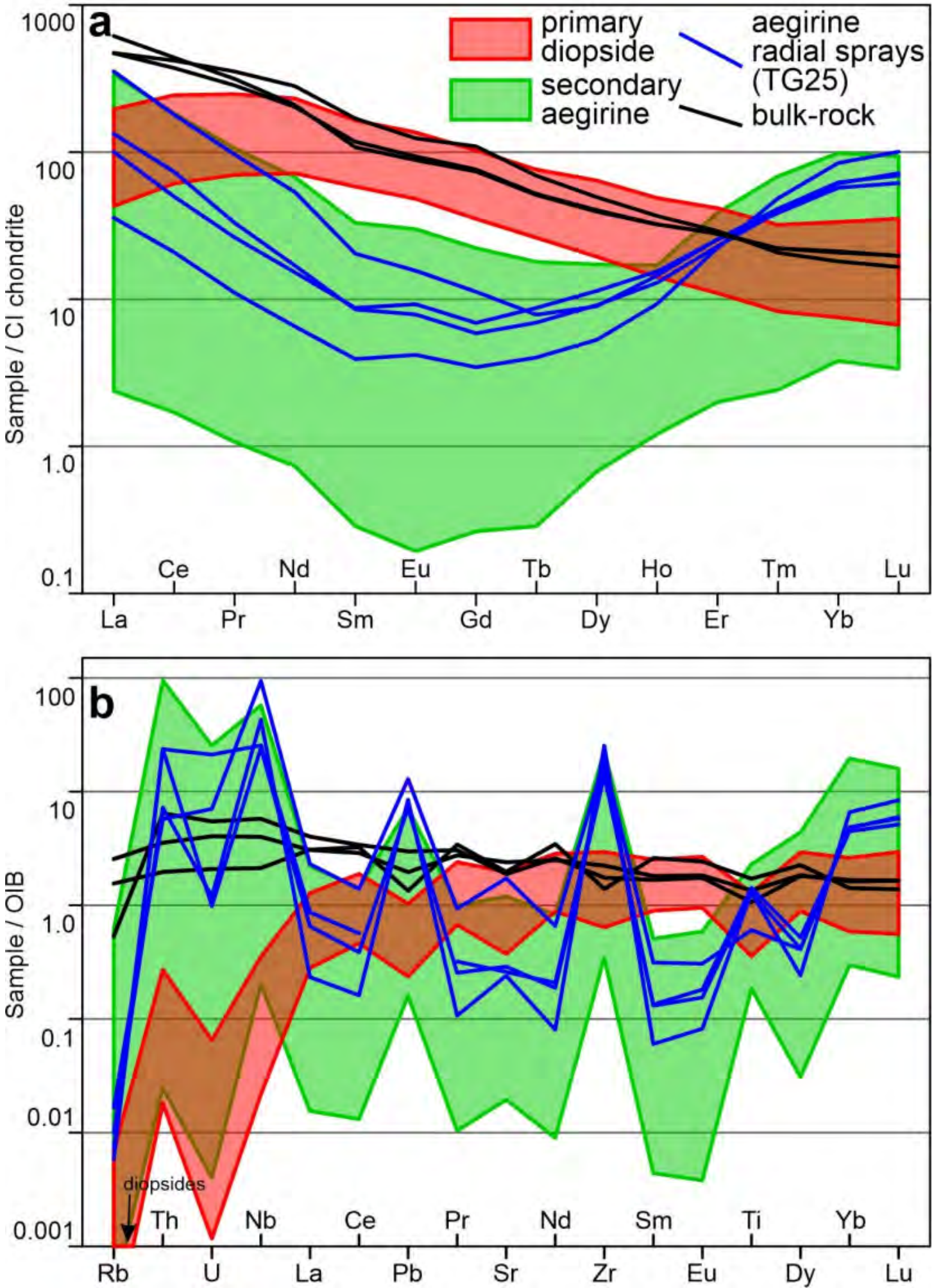
a
primary diopside
secondary aegirine
aegirine radial sprays (TG25)
bulk-rock
Sample / CI chondrite
1000
100
10
1.0
0.1
La
Ce
Pr
Nd
Sm
Eu
Gd
Tb
Dy
Ho
Er
Tm
Yb
Lu
b
Sample / OIB
100
10
1.0
0.1
0.01
0.001
diopsides
Rb
Th
U
Nb
La
Ce
Pb
Pr
Sr
Nd
Zr
Sm
Eu
Ti
Dy
Yb
Lu

Fig. 9

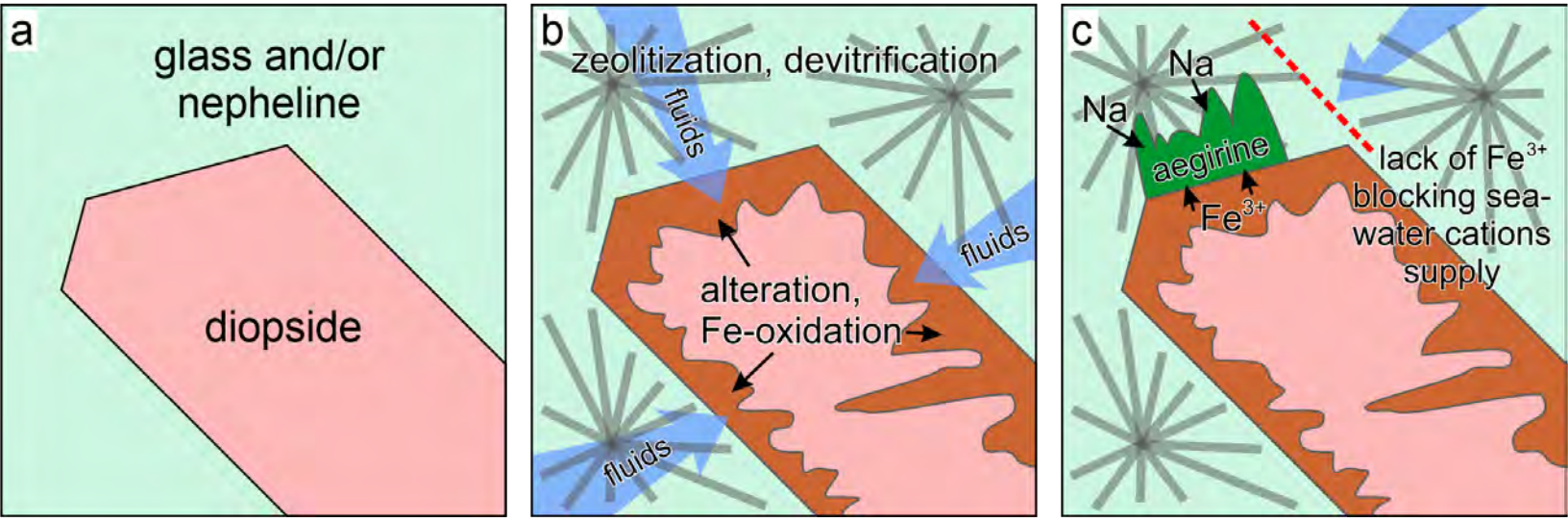
a
glass and/or
nepheline
diopside
b
zeolitization, devitrification
fluids
fluids
alteration,
Fe-oxidation
fluids
c
Na
Na
aegirine
Fe3+
lack of Fe3+
blocking sea-
water cations
supply